

1 **Title**

2 Towards HCP-Style Macaque Connectomes: 24-Channel 3T Multi-Array Coil, MRI Sequences and
3 Preprocessing

4

5 **Authors**

6 Joonas A. Autio¹, Matthew F. Glasser^{2,3,4}, Takayuki Ose¹, Chad J. Donahue², Matteo Bastiani^{5, 6},
7 Masahiro Ohno¹, Yoshihiko Kawabata⁷, Yuta Urushibata⁸, Katsutoshi Murata⁸, Kantaro Nishigori^{1,9},
8 Masataka Yamaguchi¹, Yuki Hori¹, Atsushi Yoshida¹, Yasuhiro Go^{10,11,12}, Timothy S. Coalson², Saad
9 Jbabdi⁵, Stamatios N. Sotiropoulos^{5,6,13}, Stephen Smith⁵, David C. Van Essen², Takuya Hayashi¹

10

11 **Affiliations**

12 ¹Laboratory for Brain Connectomics Imaging, RIKEN Center for Biosystems Dynamics Research, Kobe,
13 Japan

14 ²Department of Neuroscience, Washington University School of Medicine, St Louis, Missouri USA

15 ³Department of Radiology, Washington University School of Medicine, St Louis, Missouri, USA

16 ⁴St. Luke's Hospital, St. Louis, Missouri, USA

17 ⁵Wellcome Centre for Integrative Neuroimaging - Centre for Functional Magnetic Resonance Imaging
18 of the Brain (FMRIB), University of Oxford, Oxford, United Kingdom

19 ⁶Sir Peter Mansfield Imaging Centre, School of Medicine, University of Nottingham, Nottingham,
20 United Kingdom

21 ⁷Takashima Seisakusho Co., Ltd, Tokyo, Japan

22 ⁸Siemens Healthcare Japan, Tokyo, Japan

23 ⁹Sumitomo Dainippon Pharma Co., Ltd, Osaka, Japan

24 ¹⁰Cognitive Genomics Research Group, Exploratory Research Center on Life and Living Systems,
25 National Institutes of Natural Sciences, Okazaki, Japan

26 ¹¹Department of System Neuroscience, National Institute for Physiological Sciences, Okazaki, Japan

27 ¹²Department of Physiological Sciences, School of Life Science, SOKENDAI (The Graduate University
28 for Advanced Studies), Okazaki, Japan

29 ¹³National Institute for Health Research (NIHR) Nottingham Biomedical Research Centre, Queens
30 Medical Centre, Nottingham, UK

31

32 **Keywords**

33 Macaque, Primate, Human Connectome Project, Parallel Imaging, Cortex, Resting-state, Diffusion

34

35 **Corresponding author**

36 Takuya Hayashi

37 Laboratory for Brain Connectomics Imaging

38 RIKEN Center for Biosystems Dynamics Research

39 6-7-3 Minatojima-minamimachi, Chuo-ku, Kobe 650-0047, Japan

40 Tel: 81-78-304-7140

41 Fax: 81-78-304-7141

42 E-mail: takuya.hayashi@riken.jp

43 **Abstract:**

44 Macaque monkeys are an important model species for understanding cortical organization of
45 primates, yet tools and methods for noninvasive image acquisition (e.g. MRI RF coils and pulse
46 sequence protocols) and image data preprocessing have lagged behind those developed for humans.
47 To resolve the structural and functional characteristics of the relatively thin macaque cortex, high
48 spatial, temporal, and angular resolutions are required while maintaining high signal-to-noise ratio
49 to ensure good image quality. To address these challenges, we developed a macaque 24-channel
50 receive coil for 3-T MRI with parallel imaging capabilities. This coil enabled adaptation of the Human
51 Connectome Project (HCP) image acquisition protocols to the macaque brain. We also adapted HCP
52 preprocessing methods optimized for the macaque brain, including spatial minimal preprocessing of
53 structural, functional MRI (fMRI), and diffusion MRI (dMRI). The coil provided high signal-to-noise
54 ratio and high efficiency in data acquisition, allowing four- and five-fold acceleration for dMRI and
55 fMRI, respectively. Automated parcellation of cortex, reconstruction of cortical surface, removal of
56 artefacts and nuisance signals in fMRI, and distortion correction of dMRI performed well, and the
57 overall quality of basic neurobiological measures was comparable with those for the HCP. The
58 resulting HCP-style in vivo macaque MRI data show considerable promise for analyzing cortical
59 architecture and functional and structural connectivity using advanced methods that have previously
60 only been available for humans.

61

62 **Highlights**

- 63 ➤ 24-channel 3T MR receive coil designed for the smaller macaque brain.
64 ➤ In vivo macaque imaging protocols adapted according to guidelines from the HCP.
65 ➤ Parallel imaging yields five- and four-fold acceleration in fMRI and dMRI sampling.
66 ➤ HCP's minimal preprocessing and denoising pipelines adapted for macaques.
67 ➤ The multi-modal MRI data show considerable promise for HCP-style analyses.

68

69 **Introduction**

70 Old World monkeys are an important neuroscientific model for understanding primate
71 neuroanatomy (Brodmann K., 1905; Felleman and Van Essen, 1991; Van Essen et al., 2001). Macaque
72 monkeys have provided insights about neurovascular coupling (Goense and Logothetis, 2008), neural
73 wiring (Markov et al., 2014) and the evolution of the human brain's functional connectome
74 (Passingham, 2009; Wang et al., 2012). However, macaques are separated from humans by 25
75 million years of evolution, and are known to have substantial brain differences despite being
76 members of the same primate order. Recent imaging studies have revealed substantial
77 neuroanatomical differences between macaques and humans, for example in language connectivity
78 or proportion of cortex devoted to lightly myelinated association areas (Donahue et al., 2018;
79 Glasser et al., 2014; Rilling et al., 2008). At the level of cortical areas, high confidence homologies
80 (i.e., a common evolutionary origin) have only been firmly established for a modest number of early
81 sensory and motor areas (Van Essen and Dierker, 2007) but are more challenging to delineate for
82 higher cognitive regions such as prefrontal cortex (Mars et al., 2018b, 2018a). Improvements to in
83 vivo neuroimaging acquisition and preprocessing may help address several outstanding questions:
84 what is the optimal interspecies registration between macaque and human cerebral cortices? What
85 are the optimal methods for non-invasively estimating functional and structural connectivity as
86 assessed by comparison with gold standard invasive tracers in macaques? What brain networks are
87 shared and which ones are different between macaques and humans?

88

89 Recently, the Human Connectome Project (HCP) developed an improved, integrated approach to
90 brain imaging acquisition, analysis, and data sharing (Glasser et al., 2016b). The overall goal of this
91 approach is to increase the sensitivity and precision with which brain imaging studies are conducted
92 in the hope that this will yield results that are more neurobiologically interpretable and more
93 accurately comparable across individuals and studies. The HCP-style approach has seven core tenets
94 (Glasser et al., 2016b): 1) Acquire as much high-quality data from as many subjects as possible. 2)
95 Acquire data with maximum feasible resolution in space and time 3) Preserve high data quality
96 throughout preprocessing by removing physical distortions, subject movement within and between
97 scans, image intensity inhomogeneities, and artefacts and nuisance signals without blurring the data
98 or altering the neural signals (Andersson et al., 2003; Andersson and Sotiropoulos, 2016; Glasser et
99 al., 2013, 2016b, 2017; Griffanti et al., 2014; Salimi-Khorshidi et al., 2014). 4) Use appropriate
100 geometrical models—surfaces for the sheet-like cerebral cortex and volumes for globular subcortical
101 structures (Glasser et al., 2013). 5) Align brain areas across subjects, not cortical folds (Robinson et
102 al., 2018, 2014). 6) Use a data-driven structurally and functionally sensible parcellation, ideally

103 derived from multiple modalities (Glasser et al., 2016a). 7) Share results as data files in neuroimaging
104 databases such as the Brain Analysis Library of Spatial maps and Atlases (BALSA) database (Van
105 Essen et al., 2017), not just 3D coordinates. Following the HCP-Style approach leads to dramatic
106 improvements in spatial localization precision in humans relative to traditional brain imaging
107 methods (Coalson et al., 2018). Therefore, we sought to bring this improved brain imaging approach
108 to non-human primate studies.

109

110 Monkey brains present distinct imaging-related challenges relative to human brains. The macaque
111 brain is 10-fold smaller in weight, and its neocortex is ~25% thinner (average 2.0 mm vs 2.6 mm;
112 (Donahue et al., 2018; Glasser et al., 2016b)). These facts necessitate increased spatial resolution to
113 achieve comparable neuroanatomical resolution; however, smaller voxels are associated with
114 decreased signal-to-noise ratio (SNR). One way to improve SNR is to scan at ultrahigh magnetic field
115 strength (e.g., 7T). However, 7T scanners are not widely available and in any event pose technical
116 challenges such as increased B_0 and B_1 inhomogeneity (Van de Moortele et al., 2009). For
117 conventional 3T scanners, one key factor to enable high-resolution whole-brain imaging in macaques
118 is to optimize the multi-channel radiofrequency (RF) receiver coil. Using a coil matched to macaque
119 head size with a large number of small coil elements can yield improvements in SNR. Multi-channel
120 signal acquisition using advanced 3T research scanners in humans enables parallel imaging both in
121 the slice direction (i.e. multiband) (Moeller et al., 2010; Setsompop et al., 2012) and within the slice
122 plane (generalized auto-calibrating partially parallel acquisitions [GRAPPA]) (Griswold et al., 2002).
123 Although several studies have devised multichannel receive coils for macaque whole-brain imaging
124 at 3T (Helms et al., 2013; Janssens et al., 2013, 2013; Khachaturian, 2010) and 7T (Gilbert et al.,
125 2016; Mareyam et al., 1823), they have not to date demonstrated robust whole-brain mapping of
126 multi-modal MRI measures such as those acquired by HCP. Achieving comparable results in
127 macaques requires not only higher resolution and SNR but also low geometric distortion and signal
128 intensity inhomogeneity, and requires optimized hardware, sequences, and post-processing
129 techniques.

130

131 In this study, we designed and built a 24 channel receive coil with a geometry optimized for parallel
132 imaging of anesthetized macaque monkeys at 3T. Capitalizing on the accelerated imaging capabilities
133 of the coil, we adapted HCP-style data acquisition protocols for structural MRI (Glasser et al., 2013),
134 fMRI (Smith et al., 2013) and diffusion MRI (dMRI) (Sotiropoulos et al., 2013; Uğurbil et al., 2013) to
135 the small size of the macaque brain, as well as the HCP-style minimal spatial preprocessing and
136 denoising pipelines (Andersson and Sotiropoulos, 2016; Glasser et al., 2018, 2016a, 2013; Salimi-

137 Khorshidi et al., 2014, 2014). We generate accurate white and pial cortical surfaces, subcortical
138 segmentations, myelin maps, and cortical thickness maps from structural MRI, surface aligned fMRI
139 dense timeseries that have spatial artefacts and nuisance signals removed, resting state functional
140 networks, and diffusion-based fiber orientation estimates, example tractography connections, and
141 cortical neurite orientation and dispersion imaging (NODDI) (Zhang et al., 2012). The spatial
142 resolution of the structural and functional imaging modalities are scaled to the macaque cortical
143 thickness, thus providing comparable neuroanatomical resolution to HCP-style human imaging and
144 facilitating comparison of connectomes between macaques and humans.

145

146 **Methods and Materials**

147 Experiments were performed using a 3T clinical MRI scanner (MAGNETOM Prisma, Siemens,
148 Erlangen, Germany) equipped with 80 mT/m gradients (XR 80/200 gradient system with slew rate
149 200 T/m/s) and a 2-channel B₁ transmit array (TimTX TrueForm). The animal experiments were
150 conducted in accordance with the institutional guidelines for animal experiments and animals were
151 maintained and handled in accordance with the Guide for the Care and Use of Laboratory Animals of
152 the Institute of Laboratory Animal Resources (ILAR; Washington, DC, USA). All animal procedures
153 were approved by the Animal Care and Use Committee of the Kobe Institute of Riken (MA2008-03-
154 11). We also used HCP data as a reference for data quality. The use of HCP data was approved by the
155 institutional ethical committee (KOB-IRB-16-24).

156

157 *Macaque 24-channel coil*

158 The coil frame geometry was designed using a 3D digital design software (Rhino 5, McNeel,
159 Seattle, USA) to closely fit the head geometry of the animal with largest head dimensions (anterior
160 posterior 109 mm, left-right 99 mm, superior-inferior 84 mm) (Fig. 1A) in our macaque head MRI
161 database. The database included structural scans of 133 individual subjects from three macaque
162 species (*Macaca fuscata*, N=4; *Macaca fascicularis*, N=122; *Macaca mulatta*, N=7). The largest
163 animal's MRI data was used to delineate the contour of the head surface and imported into the 3D
164 digital design software where the inner surface of the coil was designed to closely fit the surface of
165 the head (Fig. 1A). Next, 16 pentagonal and 8 hexagonal elements were configured over the surface
166 (Fig. 1B), resembling a soccer-ball coil design (Wiggins et al., 2006). These elements were arranged in
167 three quasi-horizontal arrays to maximize parallel encoding power of multiband EPI sequences for
168 animals placed in the supine position and axial slices. The inner body of the device was constructed
169 using a 3D printer (M200, Zortrax, Olsztyn, Poland) (Fig. 1C), and the coil elements were arranged
170 over its external surface. Initially the coil elements were wired using a thin copper foil-plate (width 5

171 mm); however, because the plate elements markedly interfered with B_1 transmission (data not
172 shown), the coil elements were rewired using thin coaxial copper cables (Fig. 1D, cable diameter 0.7
173 mm; cable loop maximum mean diameter 48.6 ± 8.7 mm) (Wiggins et al., 2009), which substantially
174 reduced interference with B_1 transmission. The elements were arranged to continuously (critically)
175 overlap each other to reduce coupling between nearest-neighbor coils (Roemer et al., 1990), and
176 those in the caudal-posterior part were designed to have relatively larger diameter (35% larger in
177 maximum diameter) to increase sensitivity to distant brain regions (e.g. cerebellum) while reducing
178 sensitivity to closer regions (e.g. occipital cortex). The two elements placed over the eyes were also
179 relatively large in diameter to allow video recording of eyes and eyelids for monitoring depth of
180 anesthesia. In addition, capacitors were arranged vertically against the surface of the coil frame to
181 reduce interaction with B_1 -transmission (Fig. 1D). Fig. 1E shows the circuits, which followed a
182 standard design (Wiggins et al., 2006) consisting of diode detuning trap, cable trap and bias T
183 connected to low input-impedance preamplifiers (Siemens Healthcare, Erlangen, Germany). The
184 completed coil is shown in Fig. 1F.

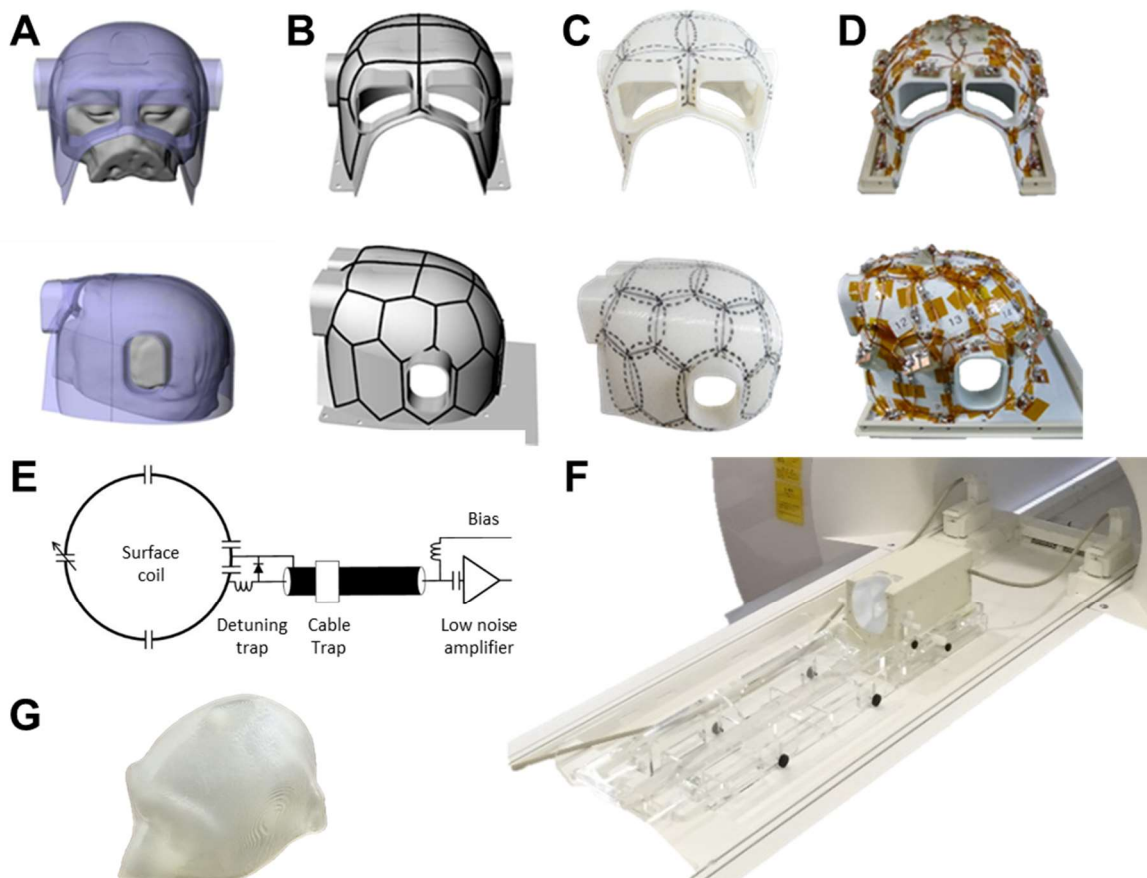


Figure 1 The design and development of macaque 24-channel receive-only coil. **(A)** Design of coil geometry and **(B)** element locations. **(C)** Outlook of element alignment on a 3D print. **(D)** Coil with final element arrangements. **(D)**

Schematic of a coil element circuit. (E) Coil circuitry. (F) Coil outlook with animal holder attached to the gantry of the MRI scanner. (G) Macaque head phantom.

185

186 *Coil Evaluation*

187 Coil elements were assessed for the ratio of loaded to unloaded quality factor Q , nearest-neighbor
188 coupling, and active detuning. Element coupling was also estimated with gradient off-line noise
189 correlation measurements. Two phantoms (NaCl 0.9%, gadolinium 0.1 mM) were designed and
190 prepared using a 3D printer: one to closely match the inner-surface of the coil (Fig. 1G) used for B_1
191 quality evaluation and the other to match to a typical macaque brain size used for geometry-
192 dependent noise amplification. B_1 -transmission was assessed with a vendor provided flip-angle
193 sequence. B_1 -receive field was estimated using a gradient-echo sequence and by calculating the
194 signal ratio between 24-channel and body receive coils. Finally, geometry-dependent noise
195 amplification due to parallel imaging was evaluated using gradient-echo imaging and GeneRalized
196 Autocalibrating Partial Parallel Acquisition (GRAPPA) (Griswold et al., 2002) in-plane acceleration
197 factors of 2, 3 and 4.

198

199 *Data Acquisition Strategy – Resolution and Contrast Considerations*

200 To improve comparability of macaque and human brains, our data acquisition strategy sought to
201 obtain data following methodologies introduced by the HCP (3T protocols) (Glasser et al., 2016b,
202 2013; Smith et al., 2013; Sotiropoulos et al., 2013; Uğurbil et al., 2013). To accurately model the
203 cortical pial and white matter surfaces, structural imaging spatial resolution target (0.5 mm isotropic
204 in macaques, equivalent to 0.8mm in humans) was based on preliminary evaluations of macaque
205 cortical thickness (Glasser et al., 2014) and corresponds to approximately half of the minimum
206 cortical thickness in the cortex, which is ≈ 1 mm in macaques (Donahue et al., 2018) and 1.6 mm in
207 humans (Glasser et al., 2016b). Tissue contrast (grey and white matter and CSF) associated imaging
208 parameters (e.g. inversion time, flip angle, repetition time and echo-time) were experimentally
209 adjusted to produce robust surface estimation within the FreeSurfer pipelines, in conjunction with
210 maximizing intracortical $T1w/T2w$ (myelin-related) contrast. The fMRI spatial resolution selection
211 (1.25 mm) was based on preliminary evaluations of the 5th (low) percentile of cortical thickness, a
212 similar strategy in humans by the HCP (resolution of 2 mm) (Glasser et al., 2016b). The temporal
213 sampling rate (TR=0.75 sec) was maximized according to tSNR (see below) which was close to the
214 human protocol (0.72 sec; Smith et al., 2013). For dMRI, the smallest spatial resolution within the
215 practical limitation of the SNR was chosen using the same b-value scheme ($b = 1000, 2000$ and 3000
216 s/mm^2) as in the HCP (Sotiropoulos et al., 2013) with 500 directions (more than the 270 in the HCP).
217 Pilot studies for each modality included assessments for varying spatial resolution, flip-angle, RF

218 transmission power, pulse length, inversion time (TI), fat suppression, multiband acceleration factor,
219 in-plane acceleration factor, repetition time (TR), echo-time (TE), echo-spacing, spectral width,
220 phase encoding direction, phase partial Fourier, phase oversampling, image resolution and diffusion
221 directions.

222

223 *Structural Acquisition Protocol*

224 T1w images were acquired using a 3D Magnetization Prepared Rapid Acquisition Gradient Echo
225 (MPRAGE) (Mugler and Brookeman, 1990) sequence (0.5 mm isotropic, FOV=128x128x112 mm,
226 matrix=256x256 slices per slab=224, coronal orientation, readout direction of inferior (I) to superior
227 (S), phase oversampling=15%, averages=3, TR=2200 ms, TE=2.2 ms, TI=900 ms, flip-angle=8.3°,
228 bandwidth=270 Hz/pixel, no fat suppression, GRAPPA=2, turbo factor=224 and pre-scan
229 normalization). The value of TI (900 ms) was selected based on the contrast between white and grey
230 matter and SNR. T2w images were acquired using a Sampling Perfection with Application optimized
231 Contrast using different angle Evolutions (SPACE) sequence (Mugler et al., 2000) (0.5 mm isotropic,
232 FOV=128x128x112mm, matrix=256x256, slice per slab=224, coronal orientation, readout direction I
233 to S, phase oversampling=15%, TR=3200 ms, TE=562 ms, bandwidth=723 Hz/pixel, no fat
234 suppression, GRAPPA=2, turbo factor=314, echo train length=1201 ms and pre-scan normalization).
235 The total acquisition time for structural scans was 22 min (17 min for T1w and 5 min for T2w).

236

237 *Functional Acquisition Protocol*

238 To reduce susceptibility induced geometric distortions and signal loss, the data was acquired in LR
239 and RL directions. Functional scans were acquired using gradient-echo EPI (FOV=95x95 mm,
240 matrix=76x76, 1.25 mm isotropic, interleaved slice order, and number of slices=50 covering the
241 whole brain).

242

243 An empirical estimate of the effect of multiband slice acceleration factor on fMRI tSNR was obtained
244 by a procedure similar to that used by the HCP (Smith et al., 2013). Briefly, simultaneous slice
245 excitation enables a multiband factor fold reduction in the TR and subsequent incomplete T1-
246 recovery leads to a reduction in the optimal (Ernst) flip angle and thus in tSNR. However, as more
247 data volumes can be acquired in a matched time window, a more relevant estimate for the data
248 quality can be calculated by multiplying the tSNR with a square root of acquired data timepoints.
249 Therefore, tSNR was estimated with a matched image acquisition time (10 min) using a range of
250 multiband factors (1, 3, 5, 6 and 8), minimum excitation and refocus RF-pulse lengths (with constant

251 spectral width), TRs (3850, 1300, 840, 680 and 530 ms), corresponding (blood) Ernst angles (86, 65,
252 55, 51 and 45°) and a fixed bandwidth (1370 Hz/pixel).

253

254 These trials led us to select the imaging parameters (multiband factor=5, TR=755 ms, number of
255 slices=45, flip-angle=55°, TE=30 ms, bandwidth=1370 Hz/pixel and echo spacing=0.95 ms and pre-
256 scan normalization) for the fMRI data acquisition. To maintain the temporal autocorrelation
257 structure of the data, long continuous runs were used (single-run scan time 51 min, 4096 frames, RL
258 and LR directions resulting in a total acquisition time of 102 min).

259

260 *Field-Map Acquisition Protocol*

261 The B_0 field-map was estimated using a pair of spin-echo EPI images with opposite phase encoding
262 directions (Andersson et al., 2003) (LR and RL directions, FOV=95x95 mm, 1.25 mm isotropic
263 resolution, axial orientation, slices=45, interleaved data acquisition, TE=46.2 ms, 6/8 phase partial
264 Fourier, bandwidth=1370 Hz/pixel, echo spacing=0.95 ms, fat suppression and pre-scan
265 normalization). The B_1 transmit field-map was obtained using vendor provided flip-angle sequence
266 (Siemens, B_1 -map) (FOV=128x128x58mm, gap=2 mm, gaps acquired in a separate run, 2 mm
267 isotropic, TR=10 s, target flip-angle=90°).

268

269 *Diffusion Acquisition Protocol*

270 Diffusion scans were acquired with a 2D spin-echo EPI Stejskal-Tanner sequence (Stejskal and
271 Tanner, 1965), utilizing monopolar gradient scheme and gradient pre-emphasis to reduce eddy
272 currents. The monopolar gradients allowed decreased TE and significantly improved SNR without
273 significant degradation due to eddy currents (in part due to the correction for eddy currents in post
274 processing) (Andersson et al., 2003). The diffusion scheme contained three shells with b-values of
275 1000, 2000 and 3000 s/mm^2 (diffusion time=26.5 ms, gradient duration=17.8 ms and amplitude=69.7
276 T/m), in accordance with the HCP (Sotiropoulos et al., 2013), but the number of direction (N_D) was
277 increased to 500 uniformly distributed over the sphere, as compared with that in the HCP ($N_D=270$).
278 Furthermore, 52 $b=0 s/mm^2$ volumes were evenly distributed across the diffusion scheme to reduce
279 CSF pulsation related uncertainty in the $b=0 s/mm^2$ image signal intensity. In contrast to the HCP, we
280 used GRAPPA (acceleration factor= 2) to reduce image distortions and accelerate the sequence in
281 plane with a more recent version of the multiband sequence than was available for the original
282 young adult HCP (Uğurbil et al., 2013). To correct for geometric distortions, the diffusion scheme
283 was obtained using two scans with reversed phase encoding directions (LR and RL) and different
284 number and directions of diffusion gradient (252 and 248) (Andersson and Sotiropoulos, 2016). The

285 following imaging parameters were applied: FOV=90 mm, matrix=100×100, 0.9 mm isotropic
286 resolution, number of slices=60, interleaved slice acquisition, multiband factor=2, GRAPPA= 2,
287 TR=3400 ms, flip-angle=90, TE=73 ms, 6/8 phase partial Fourier, echo spacing=1.12 ms,
288 bandwidth=1086 Hz/pixel, pre-scan normalization on and fat suppression using gradient reversal
289 technique (Gomori et al., 1988). Total acquisition time was 30 min, during which frequency drift was
290 small (≈ 0.5 Hz/min). By applying slice and in-plane accelerations (2×2), the acquisition time was
291 reduced by more than 3-fold than without acceleration. However, the shortest possible TR was not
292 used, in order to preserve SNR (to allow near-complete longitudinal magnetization recovery).

293

294 *Animal experiments*

295 Macaque monkeys (mean 5380 g, range 3030–8850 g) were initially sedated with intramuscular
296 injection of dexmedetomidine (4.5 $\mu\text{g}/\text{kg}$) and ketamine (6 mg/kg). A catheter was inserted into the
297 caudal artery for blood-gas sampling, and tracheal intubation was performed for steady controlled
298 ventilation using an anesthetic ventilator (Cato, Drager, Germany). End-tidal carbon dioxide was
299 monitored and used to adjust ventilation rate (0.2 to 0.3 Hz) and end-tidal volume. After the animal
300 was fixed in an animal holder, anesthesia was maintained using intravenous dexmedetomidine (4.5
301 $\mu\text{g}/\text{kg}/\text{hr}$) and 0.6 % isoflurane via a calibrated vaporizer with a mixture of air 0.75 L/min and O₂ 0.1
302 L/min. Rectal temperature (1030, SA Instruments Inc., NY, USA) and peripheral oxygen saturation
303 and heart rate (7500FO, NONIN Medical Inc., MN, USA) were monitored throughout experiments.
304 For diffusion imaging the level of isoflurane was increased to 1.0 % to reduce potential eye and head
305 motion artefacts.

306

307 *Data analysis*

308 Data analysis utilized a version of the HCP pipelines with some customized specifically for use with
309 non-human primates including structural (PreFreeSurfer, FreeSurferNHP (instead of FreeSurfer) and
310 PostFreeSurfer), functional (fMRIVolume, fMRISurface) and diffusion preprocessing
311 (DiffusionPreprocessing) (Donahue et al., 2016; Glasser et al., 2013). These NHPHCP pipelines
312 requires FMRB's Software Library (FSL) v6.0.1, FreeSurfer v5.3.0-HCP and Connectome Workbench
313 v1.3.2 (<https://www.humanconnectome.org/software/get-connectome-workbench>) and are
314 available at <https://github.com/Washington-University/NHPPipelines>.

315

316 *Structural Image Processing*

317 Preprocessing began with the PreFreeSurfer pipeline, in which structural T1w and T2w images were
318 registered into an anterior-posterior commissural (AC-PC) alignment using a rigid body

319 transformation, non-brain structures were removed, T2w and T1w images were aligned using
320 boundary based registration (Greve and Fischl, 2009), and corrected for signal intensity
321 inhomogeneity using B_1 - bias field estimate. Next, data was transformed into a standard “Yerkes19”
322 macaque atlas (Donahue et al., 2018, 2016) by 12-parameter affine and nonlinear volume
323 registration using FLIRT and FNIRT FSL tools (Jenkinson et al., 2002).

324

325 Then, the FreeSurferNHP pipeline reconstructed the cortical surfaces using FreeSurfer v5.3.0-HCP
326 (Fischl, 2012). This process included conversion of data in AC-PC space to a ‘fake’ space with 1-mm
327 isotropic resolution in volume with a matrix of 256 in all directions, intensity correction,
328 segmentation of the brain into cortex and subcortical structures, reconstruction of the white and
329 pial surfaces and estimation of cortical folding maps and thickness. The intensity correction was
330 performed using FMRIB’s Automated Segmentation Tool (FAST) (Zhang et al., 2001) followed by
331 scaling the whole brain intensity by a species-specific factor (=80). This process significantly
332 improved white and grey contrast particularly in the anterior temporal lobe as well as white surface
333 estimation, an effect that may be associated with the so-called ‘anterior temporal lobe problem’ in
334 pediatric brains, potentially due to less myelination in these white matter areas. We also improved
335 the subcortical parcellation training dataset for the macaque brain, and trained for 21 subcortical
336 structures: brainstem plus bilateral accumbens, amygdala, caudate, claustrum (which is not a part of
337 the default structures for human FreeSurfer), cerebellum, diencephalon, hippocampus, pallidum,
338 putamen, and thalamus (Fischl et al., 2002). The training dataset for brain mask extraction was also
339 created. After parcellating the cortical and subcortical structures with these training datasets using
340 the T1w image, the claustrum was treated as putamen, so that subsequent white surface estimation
341 accurately estimates the white surface beneath the insular cortex, as shown in the Results. The pial
342 surface was estimated using the T2w image to help exclude dura and blood vessels, similar to the
343 HCP pipeline (Glasser et al., 2013). We modified this procedure by applying an optimized value of
344 maximal cortical thickness (=10mm in ‘fake’ space, 5mm in real space like the FreeSurfer default).
345 The surface and volume data in ‘fake’ space was transformed back into the native AC-PC space, and
346 cortical thickness was recalculated in the animals’ real physical space.

347

348 The PostFreeSurfer pipeline transformed anatomical volumes and cortical surfaces into the Yerkes19
349 standard space, performed surface registration using folding information via MSMSulc (Robinson et
350 al., 2014, 2018), generated the mid-thickness surface (by averaging the white and pial surfaces),
351 generated inflated and very inflated surfaces, as well as the myelin map from the T1w/T2w ratio on
352 the mid-thickness surface. The volume to surface mapping of the T1w/T2w ratio was done using a

353 ‘myelin-style’ mapping (Glasser and Van Essen, 2011), in which a cortical ribbon mask and a metric
354 of cortical thickness were used, weighting voxels closer to the midthickness surface. Voxel weighting
355 was done with a gaussian kernel of 2 mm FWHM, corresponding to the mean cortical thickness of
356 macaque (see below). The surface models and data were resampled to a high-resolution 164k mesh
357 (per hemisphere), as well as lower resolution meshes (32k and 10k) for processing diffusion and
358 functional MRI data, respectively.

359

360 *Functional Data Processing*

361 Data were motion corrected, corrected for geometric distortions using spin echo field-map
362 correction with TOPUP (Andersson et al., 2003), registered to the structural images using the single-
363 band reference image and BBR (Greve and Fischl, 2009), normalized to grand 4D mean (=10000) and
364 masked (Andersson et al., 2003; Gonzalez-Castillo et al., 2013; Smith et al., 2013). Intensity bias field
365 correction was not done because the functional data were acquired with the pre-scan normalize
366 filter on. The cerebral cortical grey matter voxels were mapped to the surface with the partial-
367 volume weighted ribbon-constrained volume to surface mapping algorithm and voxels having large
368 deviations from the local neighborhood voxels’ coefficient of variation excluded. Data was minimally
369 smoothed at 1.25mm FWHM using geodesic Gaussian surface smoothing algorithm with vertex area
370 correction and resampled according to the folding-based registration (MSMSulc) to a standard mesh
371 in which the vertex numbers correspond to neuroanatomically matched locations across subjects.
372 The subcortical grey matter voxels were processed in the volume using 1.25mm FWHM subcortical
373 parcel-constrained smoothing and resampling. Altogether, these processes transformed the
374 functional data into a standard set of greyordinates (~10,000 [10k] vertices per hemisphere and
375 ~22,000 subcortical voxels) using the Connectivity Informatics Technology Initiative (CIFTI) format
376 (Glasser et al., 2013).

377

378 Structured temporal noise arising from imaging artefacts, motion and physiological noise was
379 reduced using a NHP version of multiple-run implementation of FMRIB’s ICA-based X-noisefier (FIX)
380 (“multi-run sICA + FIX”) (Glasser et al., 2018; Griffanti et al., 2017, 2014; Salimi-Khorshidi et al.,
381 2014). Principal component analysis (PCA) was applied to segregate data into structured and
382 unstructured sub-spaces and detect the dimensionality of the structured subspace based on
383 comparison of the data eigenspectrum with a null data eigenspectrum (a Wishart distribution). The
384 structured subspace was decomposed into statistically independent components using spatial ICA
385 and the resulting components were manually classified as “signal” or “noise”, based on their spatial
386 distribution and temporal properties (N=30) (Griffanti et al., 2017, 2014; McKeown et al., 1998). The

387 FIX classifier was then trained on this manual classification and the performance level was
388 characterized in terms of true positive rate (TPR) and true negative rate (TNR). A total of 186 spatio-
389 temporal features were extracted including species-specific vein maps in the standard space and
390 were used for training/classification. The performance of classifier was evaluated by leave-one-out
391 (LOO) accuracy testing for a range of thresholds. The de-noising procedure included linear trend
392 removal, aggressively regressing out 24 movement parameters, which included 6 parameters of rigid
393 transformation, 6 corresponding derivatives and 12 squares of these parameters, and non-
394 aggressively regressing out the noise components (Griffanti et al., 2014). Finally, unstructured noise
395 was attenuated using a Wishart filter (Glasser et al., 2016a) prior to dense connectome analyses.

396

397 Information about different categories of fMRI fluctuations were provided by HCP RestingStateStats
398 (Marcus et al., 2013) adapted for monkey. In brief, RestingStateStats quantifies total fMRI variance
399 (prior to any preprocessing) into six categories: high-pass filter, motion, artefacts and nuisance
400 signals (by FIX classification), unstructured noise (by PCA, see above), neural blood oxygenation level
401 dependent (BOLD) fluctuations (by FIX classification), and FIX-cleaned mean global timeseries. The
402 fractional contribution of each category was calculated by dividing by the total fMRI variance.

403

404 *Diffusion data processing*

405 Following the HCP pipeline (Sotiropoulos et al., 2013), the diffusion data was normalized for mean
406 intensity of the b=0 volume, corrected for distortion using a spin-echo field-map (i.e. a pair of b=0
407 volumes acquired in opposite phase), and for eddy-currents and motion using TOPUP and EDDY
408 (Andersson et al., 2003; Andersson and Sotiropoulos, 2016). The images were then registered to the
409 T1w structural image using the undistorted b=0 volume and a 6-DOF boundary-based registration
410 (Greve and Fischl, 2009), transformed into 0.9 mm structural volume AC-PC space (spline
411 interpolation), and masked with a brain mask. The diffusion gradient vectors were rotated according
412 to the rotational information of the rigid transformation matrix from the b=0 to T1w volume. The
413 quality of the diffusion data was assessed using 'eddyqc' in FSL (Andersson and Sotiropoulos, 2015;
414 Bastiani et al., 2019). Summary quality metrics consists of SNR calculated for the b=0 images by
415 average intensity divided by standard deviation of b=0 volumes (n=52), and for each b-value with
416 diffusion angular CNR, i.e. the ratio between the standard deviation of the signal predicted by eddy
417 using a Gaussian Process and the standard deviation of the residuals.

418

419 Fiber orientation estimation was performed with a model-based parametric deconvolution approach
420 to estimate three crossing fibers per voxel using 'bedpostx_gpu' in FSL (Behrens et al., 2007;

421 Hernández et al., 2013; Hernandez-Fernandez et al., 2018) with a burn in period of 3000 and a
422 zeppelin deconvolution kernel (Jbabdi et al., 2012; Sotiropoulos et al., 2016). The uncertainty in the
423 estimated fiber orientations in white matter voxels was compared with the respective uncertainty
424 obtained when using HCP data, for each of three crossing fibers (orientations sorted based on
425 identified volume fraction). Probabilistic tractography was performed on the fiber orientation
426 estimates using FSL's 'probtrackx2_gpu' algorithm (Hernandez-Fernandez et al., 2018) to generate
427 dense diffusion connectomes (Donahue et al., 2016). In brief, we used vertices in the white matter
428 surface and voxels in the subcortical grey matter as a seed of tracking. Streamlines were allowed to
429 propagate within subcortical regions, but they were terminated on exit (Smith et al., 2012). The pial
430 surface and a curvature threshold of 90 degrees were used as stopping criteria. The brain mask
431 calculated in FreeSurfer was used for a waypoint mask through which paths were kept. The step
432 length was set to 0.23 mm, one fourth of voxel size, and the maximum path length to 200 mm. The
433 calculated dense connectomes were created by counting the number of streamlines that terminal on
434 voxels within the seed regions and normalizing by the total number of generated streamlines. These
435 dense connectomes were parcellated using the M132 cortical areas (Markov et al., 2014) to reduce
436 gyral bias and the parcellated connectome matrices were fractionally scaled, symmetrized, and \log_{10} -
437 transformed (Donahue et al., 2016). The quality of the dMRI data and the success of the tracking
438 algorithm were evaluated with respect to quantitative retrograde tracer data by correlating \log_{10} -
439 transformed tractography with the corresponding \log_{10} -scaled fraction of labeled neurons in a
440 source area relative to the total number of label neurons extrinsic to the injected area (Donahue et
441 al., 2016; Markov et al., 2014). Cortico-cortical pathways that did not exhibit connectivity in the
442 retrograde tracer were excluded from the analysis.

443

444 Neurite orientation dispersion and density imaging (NODDI) was used to evaluate tissue
445 microstructure associated with neurite composition (a collective term referring to both dendrites
446 and axons) (Zhang et al., 2012). Briefly, NODDI models three compartments (intra-cellular, extra-
447 cellular and CSF) each with different diffusion properties (stick-tensor-ball model), where the
448 diffusion motion in the intra-cellular compartment is assumed to be restricted to within neurites
449 (stick), while that in the extra-cellular compartment is assumed to be a combination of Gaussian
450 anisotropic (tensor) hindered by the presence of neurites, and Gaussian isotropic (ball) in CSF. The
451 model includes two *a priori* assumed parameters of intrinsic axial diffusivity $1.1 \mu\text{m}^2/\text{ms}$ optimized
452 for grey matter in human (Fukutomi et al., 2018), and isotropic diffusivity $3.0 \mu\text{m}^2/\text{ms}$ (Zhang et al.,
453 2012), as well as four unknown parameters (intra-cellular volume fraction, concentration parameter
454 of Watson distribution (K), mean orientation of Watson distribution (μ) and isotropic volume fraction

455 (V_{iso}). The estimated parameters of orientation dispersion index (ODI) and neurite density index
456 (NDI), as well as diffusion tensor parameters of fractional anisotropy (FA) and mean diffusivity (MD),
457 were mapped onto the cortical surface using an algorithm weighted towards the cortical mid-
458 thickness (Fukutomi et al., 2018).

459 **Results**

460 *Coil performance*

461 Coil bench tests showed that the unloaded/loaded Q ratio of the individual coil elements were
462 approximately $215/75=2.9$. This relatively low Q-ratio results from the small degree of loading and
463 small electromagnetic flux due to the small diameter of the coil elements. Decoupling between
464 adjacent elements was less than -20 dB indicating low mutual inductance between the elements.
465 This produced noise correlation coefficients averaging 0.084 (interquartile range 0.02 and 0.126)
466 with a maximum of 0.395 (see correlation matrix Fig. 2A). High noise correlation was largely
467 constrained to the nearest neighbor elements (see Fig. 1B for element geometry, see also
468 Supplementary Fig. S1 for coil channel-specific noise correlation maps).

469

470 The inverse g-factor map, a measure of coil element separation, illustrates geometry dependent
471 signal intensity variation due to parallel image reconstruction used for dMRI (Fig. 2C). A reduction
472 factor of two yields an average inverse g-ratio slightly larger than unity ($1/g=1.03 \pm 0.07$; values
473 reported throughout text as mean \pm s.d. unless otherwise specified), indicating a small noise
474 cancellation attributable to low element noise correlation and parallel image reconstruction.
475 However, larger reduction factors (R=3 and 4) yield substantial degradation of signal intensity
476 depending on geometry (Fig. 2C, D), suggesting that a maximum GRAPPA of 2 is practical for this coil.

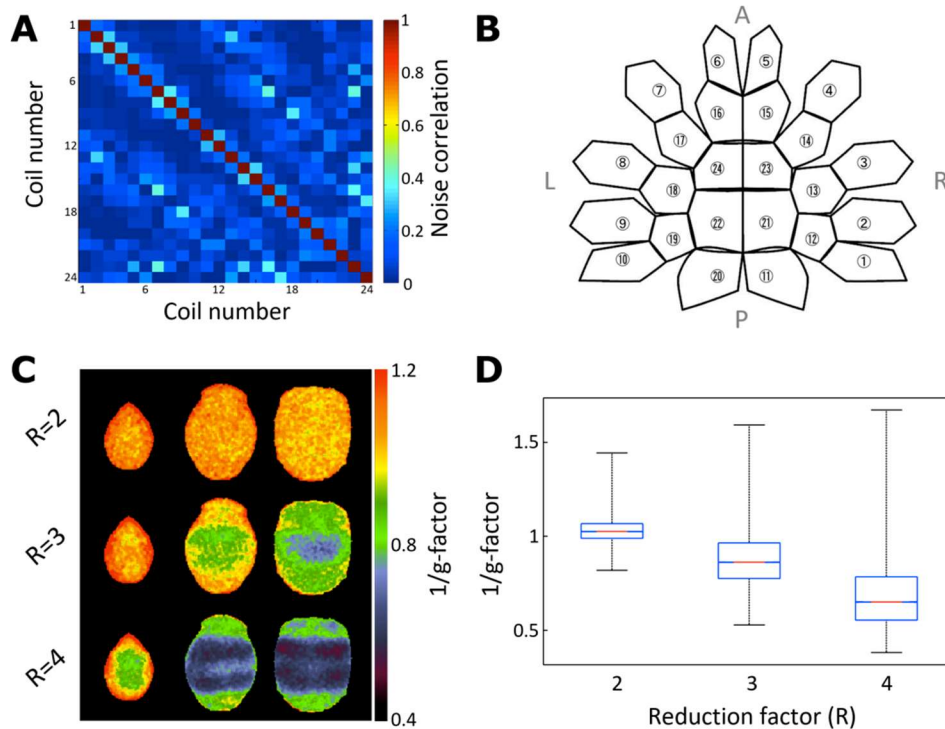


Figure 2. Macaque 24-channel coil performance and geometry. **(A)** Noise correlation matrix. **(B)** Coil element arrangement and labeling flattened into a 2D representation. **(C)** Inverse geometry ($1/g$)-factor maps using gradient

echo imaging with generalized autocalibrating partially parallel acquisitions (GRAPPA) reduction factors (R=2, 3 and 4) in LR-direction used for diffusion MRI (see later). **(D)** The boxplot shows $1/g$ -factor with respect to reduction factor. While geometric distortions are small with acceleration factor of 2 ($1/g=1.03\pm 0.07$), further reduction yields large signal degradations. Geometric distortions were evaluated using a phantom whose contour was matched to the average macaque brain.

477

478 *Macaque Data Quality Evaluation*

479 Structural bias-field corrected T1w and T2w weighted images acquired at 500- μ m resolution are
480 shown in Fig. 3A and B for an exemplar single subject. Note the good SNR and contrast of the white
481 matter to grey matter (and to CSF) throughout the brain.

482

483 Flip-angle maps indicate that the transmission was slightly higher in subcortical regions compared to
484 cortical structures (Fig. 3C), as expected. However, the surface map (Fig. 3D) indicates that the RF
485 transmission was relatively uniform over the cortical surface ($86.6^\circ \pm 2.3$) (see also Supplementary
486 Fig. S2A for phantom data). Thus, signal intensity and contrast variations at macaque cortical surface
487 attributable to RF-transmission inhomogeneity are modest.

488

489 B_0 volume (Fig. 3E) and surface (Fig. 3F) maps show inhomogeneities, particularly in and near air
490 cavities adjacent to the cerebellum and inferior temporal cortex. These inhomogeneities cause signal
491 intensity loss and spatial distortion in gradient-echo EPI images. Representative tSNR volume (Fig.
492 3G) and surface (Fig. 3H) maps, acquired with EPI at 1.25 mm isotropic resolution, provide a
493 quantitative estimate for the data quality. The mean FIX-cleaned tSNR in the macaque brain was
494 51.6 ± 25.6 overall, 67.5 ± 23.7 in the cortical ribbon and 37.3 ± 14.1 in subcortical regions. These
495 macaque tSNR values are higher than the HCP data: the FIX-cleaned tSNR in an exemplar HCP
496 subject was 38.1 ± 15.1 in the whole brain, 43.0 ± 15.2 in the cortical ribbon, and 30.7 ± 10.8 in
497 subcortical regions (Supplementary Fig. S3 and Table S1). However, a relatively low cortical tSNR in
498 lateral occipito-temporal cortex was notable in macaque data (Fig. 3H), which is mainly attributable
499 to a large B_0 dephasing effect (Fig. 3F).

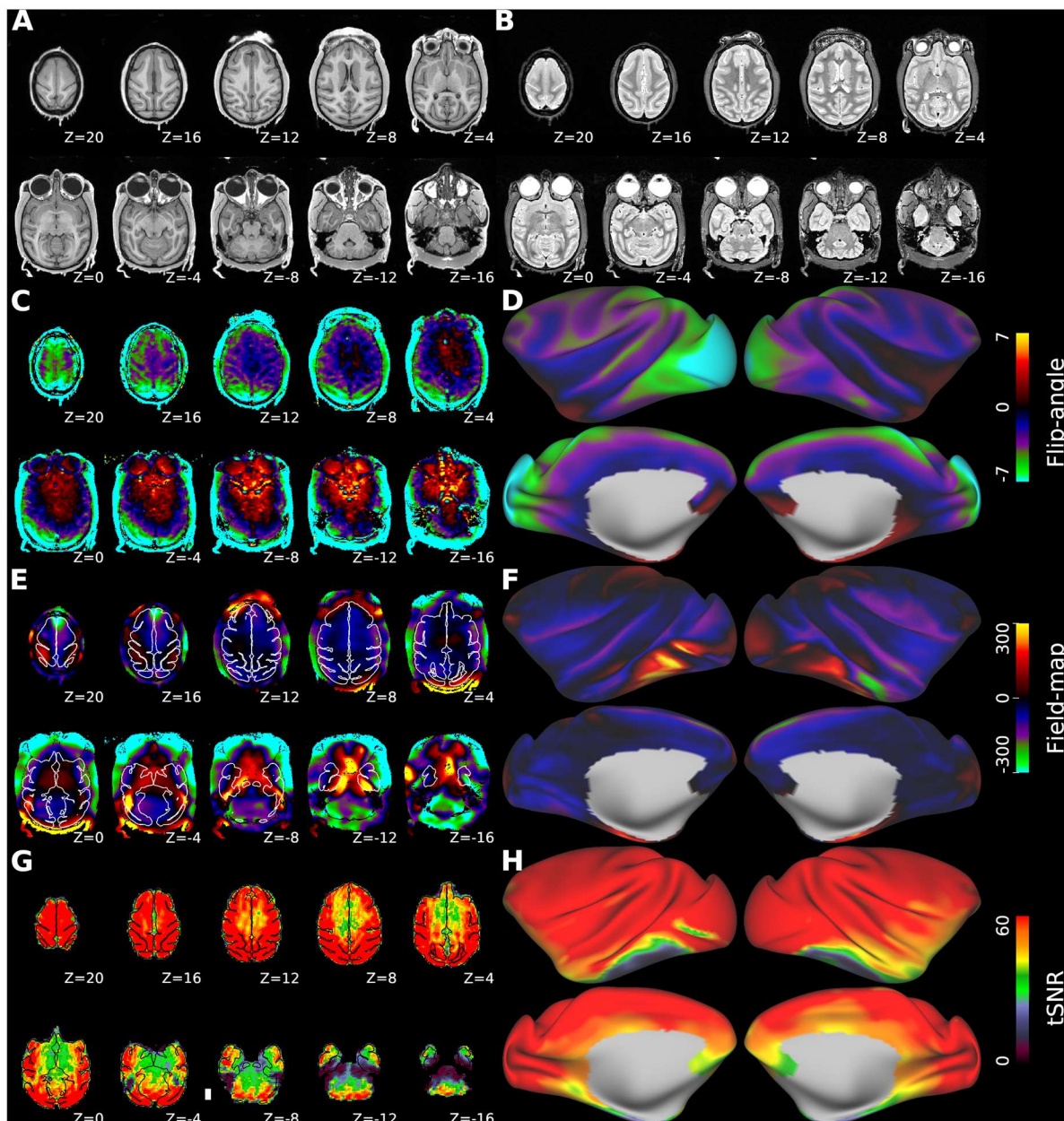


Figure 3. Data quality assessment of structural and functional MRI. Axial slices acquired with 500 μm isotropic resolution **(A)** T1-weighted MPRAGE and **(B)** T2-weighted SPAGE. Flip-angle **(C)** axial and **(D)** surface maps. The values indicate the difference between experimental and nominal flip-angle (90°) in units of degree. B_0 **(E)** axial and **(F)** surface field-maps. Unit radian per second. White and black lines (in E and G, respectively) outline the pial surface. Temporal signal-to-noise ratio (tSNR) **(G)** axial and **(H)** surface maps of FIX-cleaned fMRI. The tSNR map was acquired using multiband 2D-EPI sequence (TR=0.755s, TE=30ms, MBF=5, isotropic resolution=1.25mm). Data at <https://balsa.wustl.edu/Z44X3>

500

501

502 *Single-Subject Cortical Architecture in Three Macaque Species*

503 FreeSurfer automated segmentation of cortical and subcortical structures using our NHPHCP

504 structural pipeline was reliable across the subjects (Supplementary Fig. S4B), and benefited from

505 additional signal intensity normalization (Supplementary Fig. S4A, see also Supplementary Fig. S2A

506 and S2B for B_1 -transmit and receive fields, respectively). Inspection of pial and white matter surface

507 contours indicates that the automatic segmentation generally followed the contrast boundaries of

508 the T1w image (Supplementary Fig. S4C) and the T2w image (Supplementary Fig. S4D) appropriately,
509 including in challenging thin heavily myelinated regions such as early visual and somatosensory
510 cortex. The subcortical structures including claustrum, pallidum, putamen, were automatically and
511 accurately segmented by the improved subcortical atlas (Supplementary Fig. S4B). The newly added
512 intensity normalization improved the problematic estimation of the white matter surface in the
513 anterior temporal lobe (Supplementary Fig. S5A right), which was not achieved using the default
514 intensity bias field correction (Supplementary Fig. S5A left). The claustrum parcellation strategy also
515 improved the white matter surface just beneath the insular cortex (Supplementary Fig. S5B, right),
516 which often resulted in ‘claustrum invagination’ of the white surface by the default FreeSurfer
517 (Supplementary Fig. S5B left). The claustrum parcellation also improved myelin contrast in the
518 anterior insular area (see next paragraph).

519

520 Fig. 4 shows representative cortical surface mapping for three macaque species: Japanese rhesus
521 monkey (*M. fuscata*), rhesus monkey (*M. mulatta*) and crab-eating monkey (*M. fascicularis*), as well
522 as for average of three species (N=12, consisting of N=4 for each species). Although the brain size
523 and surface area were different across species and individuals, we successfully achieved cortical and
524 subcortical parcellation by applying the same Gaussian Classifier Atlas (GCA) and obtained the
525 surface estimation on gyral and sulcal formations (Fig. 4A-H), myelin contrast (Fig. 4I-L), which were
526 comparable across species. The total cortical surface area per hemisphere (excluding the non-
527 cortical ‘medial wall’) ranged from 8,093 to 12,897 mm² with an average of 10,052 ± 1,584 mm²
528 (number of hemispheres=24). The average myelin map (Fig. 4L) showed relatively high values in
529 primary visual, sensorimotor and auditory regions and in the “MT+” complex, whereas association
530 areas show relatively low values. These results for myelin maps are in good agreement with each
531 other and with published group average macaque maps (Donahue et al., 2018; Glasser et al., 2014;
532 Glasser and Van Essen, 2011). However, the myelin level in anterior insular cortex tended to be low
533 relative to these earlier maps (Glasser et al., 2014); we consider the present maps likely to be more
534 accurate since this region of agranular insular cortex is very lightly myelinated (Mesulam and
535 Mufson, 1982). Our maps likely benefitted from improved segmentation between claustrum and
536 insular cortex, as described above.

537

538 Cortical thickness maps were reasonably consistent across three macaque species (Fig. 4M-P). Most
539 of frontal, anterior insular and temporal cortices are relatively thick, whereas most of visual and
540 parietal cortices are relatively thin. Histograms indicate the distribution of cortical thickness (Fig. 4Q-
541 T). Average cortical thickness across species was 2.1 ± 0.54 (median 2.0, N=12). The (lower) fifth

542 percentile of the cortical thickness, evaluated from species average, was 1.38 mm. These estimates
543 indicate that utilizing rfMRI isotropic resolution of 1.25 mm ($\approx 2 \text{ mm}^3$) can capture voxels mainly
544 within the cortical sheet, with modest partial volume effects.
545

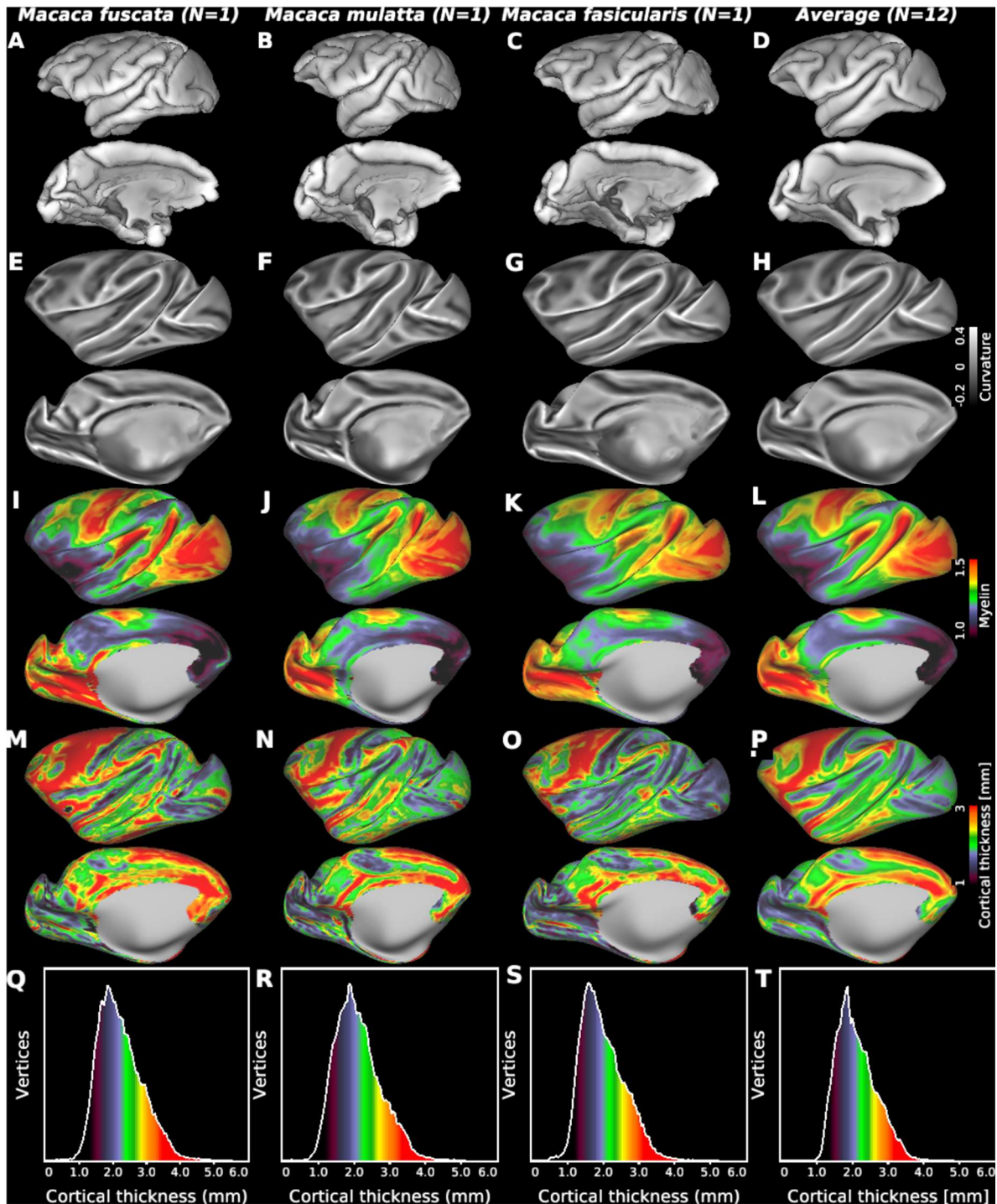


Figure 4. Cortical surface mapping of three widely studied macaque monkeys. Japanese rhesus (*Macaca fuscata*, N=1), rhesus (*Macaca mulatta*, N=1), and crab-eating monkey (*Macaca fascicularis*, N=1) and average maps across the species (N=12; N=4 for each species). (A, B, C, D) Pial surface. (E, F, G, H) Curvature and (I, J, K, L) bias-corrected myelin maps

shown on very inflated cortical surface. Cortical thickness (**M, N, O, P**) maps and (**Q, R, S, T**) histograms. Data at <https://balsa.wustl.edu/VjjZV>

546

547 *Data quality of resting-state fMRI*

548

549 To estimate the optimum multiband factor in fMRI, we determined the relationship between tSNR x
550 $\sqrt{\text{timepoints}}$ and multiband acceleration factor (Fig. 5A) and found that tSNR x $\sqrt{\text{timepoints}}$
551 increases up to a factor of 5, then decreases. This pattern was more evident after the data was
552 processed using ICA-based artefact removal algorithm FIX, which yielded approximately 25%
553 improvement in tSNR. In the cortical ribbon, denoised tSNR x $\sqrt{\text{timepoints}}$ is clearly highest at
554 MBF=5 (Fig. 5B).

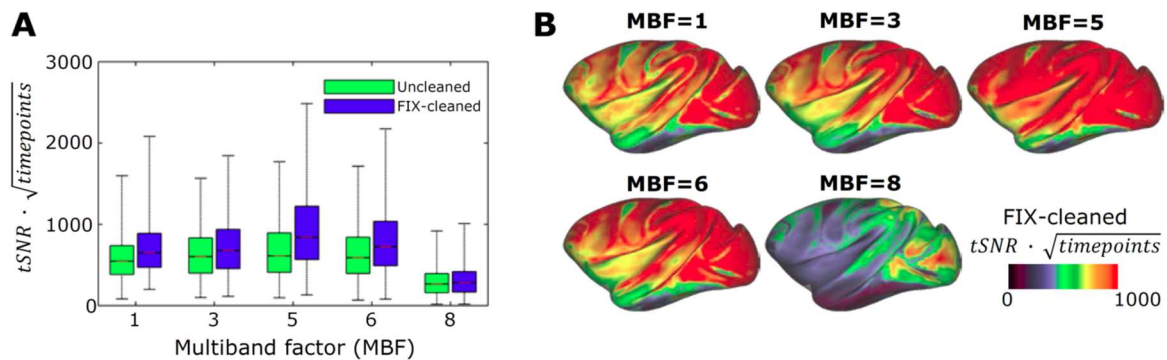


Figure 5. Optimization of fMRI multiband acceleration. **(A)** Relationship between temporal signal-to-noise ratio (tSNR) multiplied by a square-root of acquired time-points and multiband factor (MBF). Acquisition times are matched in the data points (each scan 10 minutes, N=1). The boxplot shows distributions of tSNR in the greyordinates (a total of 26k) for FIX-uncleaned (green) and FIX-cleaned data (blue). **(B)** Cortical surface presentation of FIX cleaned tSNR x $\sqrt{\text{timepoints}}$ vs multiband factor. Note that MBF=5 produces the highest tSNR.

555

556 The resting-state fMRI runs were analyzed using multi-run sICA + FIX. The resulting sICA components
557 (a total of number of components: 124 ± 29 for each animal, N=30) were manually classified as noise
558 (on average 100 ± 23 components per animal) or signal (24 ± 9 components per animal). The manual
559 classification worked well to train FIX, and the classification accuracy achieved reasonably high
560 performance (Table 1). The LOO accuracy testing showed that mean TPR and TNR ranged between
561 96.9-99.9% and 95.1-99.6%, respectively, depending on the choice of threshold. A threshold of 20 was
562 used for classification, which resulted in mean TPR and TNR of 99.0% and 98.8%.

563

564 **Table 1.** FIX classification accuracy tested by leave-one-out (LOO) in thirty anesthetized macaque
565 data. Abbreviations: TPR=true positive rate of signal components and TNR=true negative rate of true
566 artefact components.

FIX threshold	1	2	5	10	20	30	40	50
TPR (mean)	99.9	99.9	99.7	99.6	99.0	98.3	97.4	96.9
TNR (mean)	95.1	96.1	97.4	98.2	98.8	99.0	99.3	99.6
TPR (median)	100	100	100	100	100	100	100	100
TNR (median)	96.1	96.4	97.8	98.6	98.9	99.1	99.6	100

567

568 Using RestingStateStats in HCP Pipeline (Glasser et al., 2018; Marcus et al., 2013), the variance in
 569 macaque resting-state fMRI runs was divided into six categories. Fig. 6 shows their relative
 570 contributions to the total signal variance ($38,400 \pm 13,000$, $N=20$, see also Table S2). Relative
 571 variance estimations in descending order were unstructured noise ($70.0 \pm 4.8\%$), high-pass filtered
 572 noise ($15.3 \pm 4.5\%$), structured noise (i.e. artefacts and nuisance signals, $6.0 \pm 1.5\%$), (neural) BOLD
 573 fluctuations ($4.1 \pm 2.3\%$), motion ($2.9 \pm 1.3\%$), and FIX-cleaned global signal timeseries ($1.0 \pm 0.7\%$).
 574 In comparison to HCP, unstructured noise accounted for a slightly larger portion in macaque (Fig. 6),
 575 which mainly originates from subcortical structures (see Supplementary Fig. S6 for spatial
 576 distribution of the variance categories). Furthermore, the relative BOLD contribution was smaller in
 577 macaque (4.1%) in comparison to HCP ($7.7 \pm 2.6\%$). Taken together, the contrast-to-noise ratio
 578 (CNR), defined as ratio between BOLD and unstructured signal, was smaller in macaque (0.21 ± 0.07)
 579 than in HCP (0.37 ± 0.08), which may be due to reduced BOLD signals in the anesthetized state (see
 580 section Resting-state fMRI in Discussion).

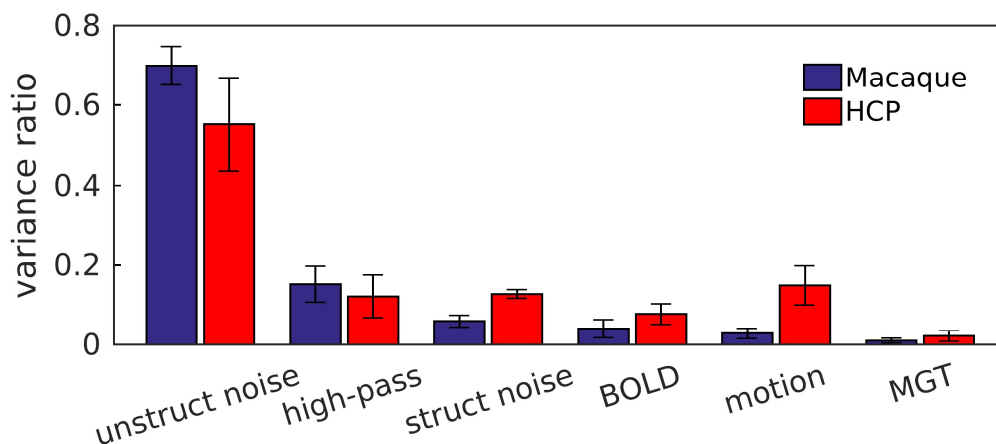


Figure 6. Classification of resting-state fMRI variance and their relative contributions of the total variance in macaque ($N=20$) and the human connectome project (HCP, $N=20$). The variances were computed using a development version of the Resting State Stats HCP pipeline. Abbreviations: struct noise=structured noise (scanner artefacts and nuisance signals etc.), BOLD='neural' blood oxygen level dependent signal, MGT=FIX-cleaned mean greyordinate timeseries.

581

582 One useful way to inspect the data quality is to visualize global (and semiglobal) artefacts in a 2-
 583 dimensional heatmap with time on x-axis and parcel (M132) timeseries on y-axis (i.e. greypplot)

584 (Glasser et al., 2018; Power, 2016; Power et al., 2014). Comparison of a representative greyplot prior
585 to any preprocessing (Supplementary Fig. S7A) and after preprocessing (Supplementary Fig. S7B)
586 demonstrated that preprocessing reduced structured artefacts. The mean global timeseries (MGT)
587 also demonstrate that FIX reduced the global signal variance, which in humans is primarily related to
588 respiration after movement artefacts have been removed by sICA+FIX. MGT power spectrum
589 (Supplementary Fig. S7C) revealed distinct peaks within the ventilation frequency range (0.25 to 0.30
590 Hz). Preprocessing effectively attenuated ventilation artefacts, but only partially attenuated the low
591 frequency, more likely neural, fluctuations (<0.1 Hz). Across subjects, the MGT variance was $2,230 \pm$
592 $1,530$ prior to preprocessing and 170 ± 110 after preprocessing (Supplementary Fig. S7D, N=20).
593 There appears to be relatively less global physiological noise in the macaque data relative to the
594 human data (Glasser et al., 2018; Power, 2016), perhaps because the animals' respiration was
595 externally controlled by the respirator.

596

597 Figure 7 shows a representative resting-state network (RSN) component and seed-based
598 connectivity obtained in a single monkey. Data was from two 51-min fMRI scans, preprocessed for
599 correction of motion, distortion, inhomogeneity, and denoising with multi-run FIX as described
600 earlier. The dense timeseries was further reduced in random noise using Wishart filtering (Glasser et
601 al., 2016a) and was used for seed-based dense connectivity by computing the full correlation. The
602 example RSN component (Fig. 7A) extended positive connectivity over posterior parietal cortex
603 (areas 7A, DP, LIP), precuneus (areas 23, 31), temporo-occipital areas (MST, PGa) and prefrontal
604 cortex (areas 46d, 8b). Temporal properties of this component included low frequency fluctuations,
605 less than 0.2 Hz, which are typical of RSNs. A similar functional connectivity pattern was found using
606 a single greyordinate seed placed over the area 7A (Fig. 7B). Both the RSN signal components (a total
607 of 32 signals) and the dense functional connectome can be interactively viewed in Connectome
608 Workbench after downloading data from the BALSAs database (<https://balsa.wustl.edu/3ggwG>).
609 Overall, these results demonstrate that our experimental setup enables robust functional
610 connectivity detection and analysis.

611

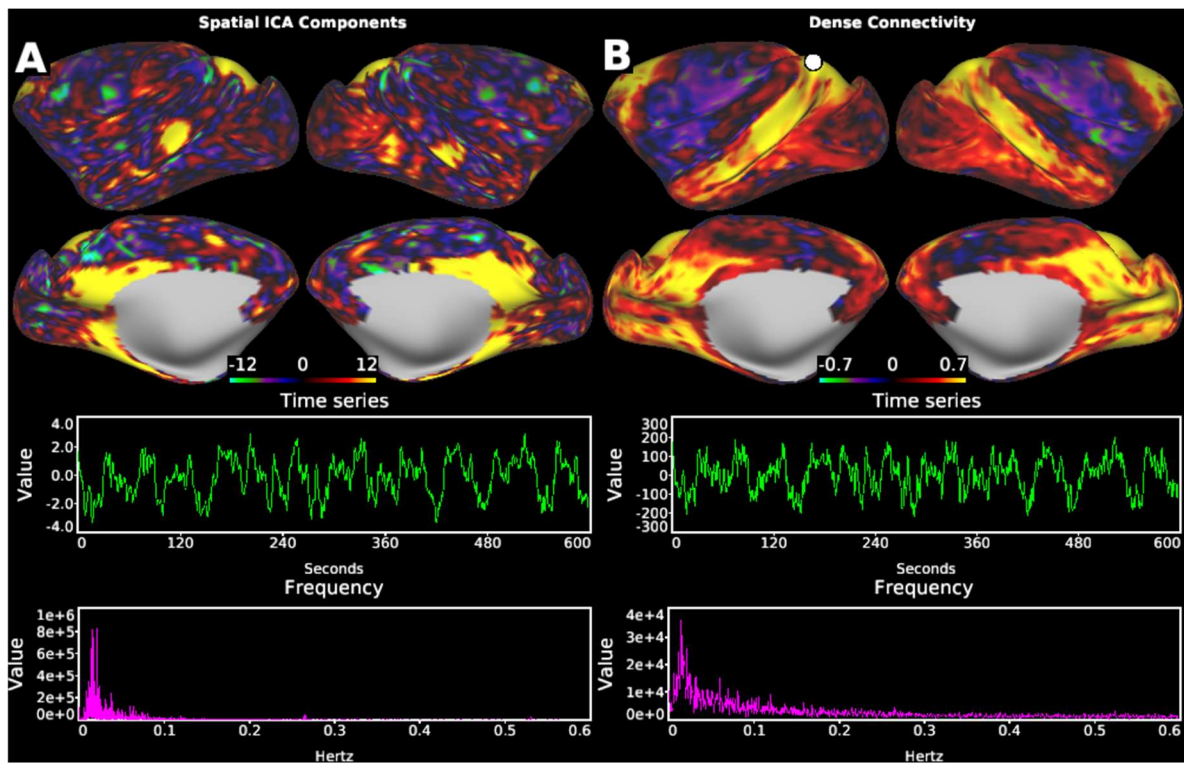


Figure 7. Representative macaque resting-state functional connectivity in a single subject. **(A)** An example resting-state network (RSN) obtained in spatial ICA, which shows positive connectivity over posterior parietal cortex (areas 7A, DP, LIP), precuneus (areas 23, 31), temporo-occipital areas (MST, PGa) and prefrontal cortex (areas 46d, 8b, as defined in M132 atlas). Timeseries and frequency of this component (lower panels) exhibited pronounced low-frequency oscillations. **(B)** Exemplar functional connectivity seeded from a single greyordinate in the area 7A (white circle). Spatial distribution of connectivity resembled to that of the component in (A), as well as timeseries and frequency of the seed signal (lower panels). Data was from two 51-min fMRI scans (subject N=1), preprocessed for correction of motion, distortion, inhomogeneity, and denoising with multi-run FIX. The dense timeseries was further reduced in random noise by Wishart filter and used for seed-based dense connectivity (Pearson's correlation). Other components classified into signal or noise, and dense connectivity seeded from other vertices can be interactively viewed using Workbench using data at <https://balsa.wustl.edu/3ggwG>

612

613 *Diffusion MRI*

614 Following the HCP paradigm, we used reversed left-right phase-encoding directions in dMRI
615 acquisition to reduce TE, TR and distortion and to increase SNR and angular CNR. An example of
616 image distortion and correction (axial and coronal views) is shown in Supplementary Fig. S8. Image
617 distortions are large near regions with large B_0 inhomogeneity (i.e. temporal lobe, see Fig. 3E, F).
618 Nonetheless, distortion correction was accurate, albeit with some signal drop-out and degraded SNR
619 in these regions. Mean motion absolute displacement during 30-min acquisition was 0.36 ± 0.07 mm
620 (N=10), ensuring little interaction between head motion, eddy-currents and changes in static
621 magnetic field. In contrast to HCP at 3T (Uğurbil et al., 2013), we used simultaneous MB and GRAPPA
622 acceleration to reduce distortions. Inspection of temporal stability of the dMRI acquisition did not

623 reveal pronounced structural artefacts around the ventricles and basal slices (Supplementary Fig.
624 S9), thus indicating that simultaneous MB and GRAPPA accelerations did not substantially interact
625 with physiological noise (Uğurbil et al., 2013). The dMRI quality assurance measures were similar
626 between this study and the HCP (Fig. 8). Average SNR (whole brain) was 11.6 ± 1.4 in macaque
627 (N=10) and 9.4 ± 0.9 in the HCP (N=10) (Fig. 8A). Exemplar subject data are compared in
628 Supplementary Fig. S10 and Supplementary Table S3. The CNR slightly increased towards higher b-
629 values and was similar across the studies (Fig. 8B). In white matter, three crossing fibers voxels
630 (selected by thresholding at 0.05 of third fiber's volume fraction) were detected in $59\% \pm 7\%$ and
631 $57\% \pm 4\%$ of voxels in macaque and the HCP, respectively (Fig 9D). Finally, the dispersion
632 uncertainties of 1st, 2nd and 3rd fiber orientations these voxels exhibited were also similar across the
633 studies (Fig 9E).
634

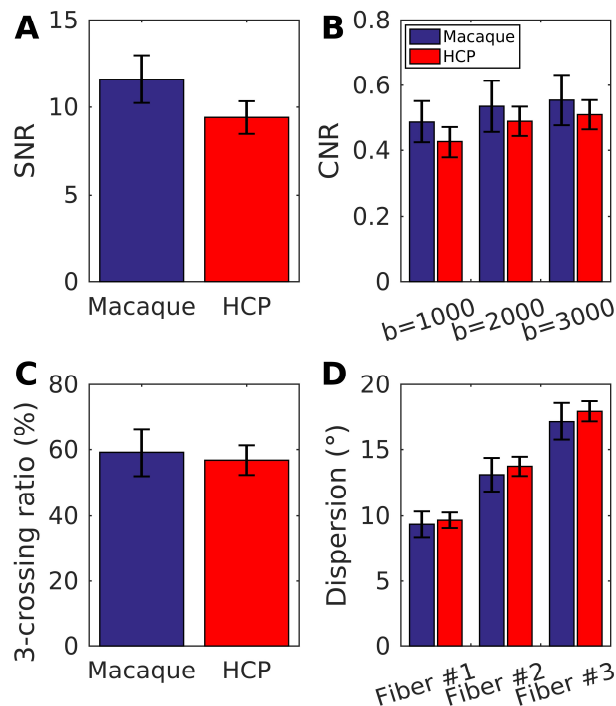


Figure 8. Comparison of dMRI quality measures between macaque and the HCP (blue and red bars, respectively; N=10). Plots show whole brain SNR (A) and CNR across b-values 1000, 2000 and 3000 (B), as well as three-crossing fiber ratio (C) and dispersion uncertainties (in degree) of 1st, 2nd and 3rd fiber orientations in the white matter voxels (D). Overall, the quality measures were comparable across the studies.

635

636 Figure 9 shows M132 parcellated cortical maps of MD (Fig. 9A), FA (Fig. 9B), NDI (Fig. 9C) and ODI
637 (Fig. 9D) (N=6). The MD is low in the primary motor (F1) and premotor cortices (such as F2, F4, F5),
638 and primary sensory cortices including somatosensory (areas 3, 1, 2), visual (V1) and auditory
639 cortices including core, as well as intraparietal sulcus area (Fig. 9A), whereas the NDI is high in all of

640 these areas. MD and NDI were strongly anti-correlated ($R=-0.75$, $p<0.001$). The ODI was high in the
641 periphery of the V1, somatosensory area 1, auditory cortices including core (Fig. 9D) and
642 intermediate in MT and other higher visual areas. The FA was higher in the frontal and anterior
643 temporal cortices and strongly anti-correlated with ODI ($R=-0.86$, $p<0.001$). These results are
644 comparable with those observed in the HCP (Fukutomi et al., 2018). The structural connectivity
645 patterns extracted from diffusion tractography (DT) were also parcellated and explored with respect
646 to the published quantitative retrograde tracer data (Fig. 9E, F) (Markov et al., 2014). Comparison
647 between parcellated DT (pDT) seed from area L-F5 and tracer data seeded from area F5 showed a
648 relatively good correlation ($R=0.70$, $p<0.001$, for non-zero tracer connections: $N=72$). However,
649 fidelity of pDT decreased for weak long-distance connections (e.g. false positive connection to MT
650 and MST and false negative connections to V2, V3, TEpd and TEpv), as reported previously (Donahue
651 et al., 2016).
652

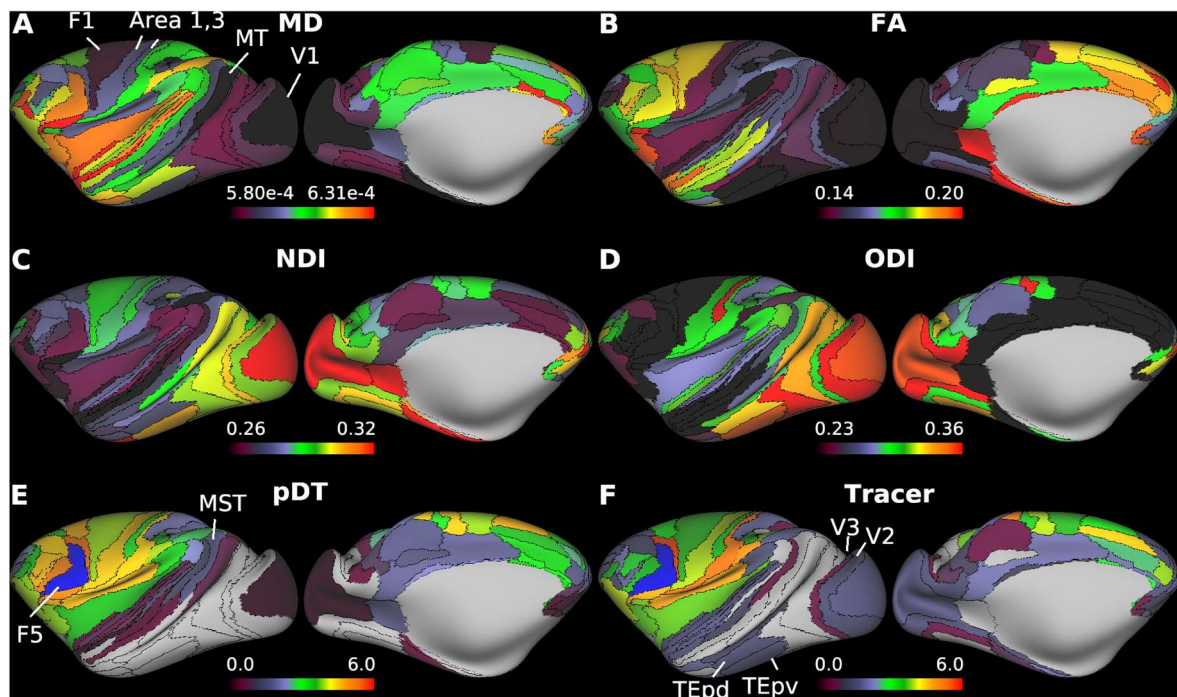


Figure 9. Representative diffusion magnetic resonance imaging (dMRI) applications. Parcellated cortical surface distributions of mean diffusivity (MD) (A) and fractional anisotropy (FA) (B) calculated in diffusion tensor model, and neurite density index (NDI) and (C) orientation dispersion index (ODI) (D) calculated in NODDI (see main text; $N=6$). (E) Parcellated diffusion tractography ($N=1$, ID=A18031601) seed from left premotor area, F5 (blue color) and (F) the quantitative ground-truth derived from retrograde tracer injected into F5. Note the correspondence between tractography and tracer connectivities (see main text for details). Data at <https://balsa.wustl.edu/zppXg>

653

654

655 **Discussion**

656 Here, we have presented an adaptation of the HCP's approach to multimodal MRI acquisition,
657 preprocessing, and analysis to the macaque, using the combination of a custom-made 24-channel
658 receive-coil, high-resolution parallel imaging, and the HCP-NHP preprocessing and analysis pipelines.
659 This approach yields robust estimates of cortical thickness, myelin content, and functional and
660 diffusion measures. Importantly, since the presented protocols used share similar strengths to the
661 HCP image acquisition, and the data is stored in a common geometrical framework system ('CIFTI
662 greyordinates'), we anticipate that it will facilitate direct multi-modal comparisons with an
663 unprecedented accuracy between macaque and human connectomes. To enable other groups to do
664 HCP-Style analyses in the macaque, this 24-channel macaque coil is available (via Rogue Research;
665 production: Takashima Seisakusho Co. Ltd., Tokyo, Japan) and the data acquisition protocols are
666 freely available from our website (www.nitrc.org/TBA), enabling other investigators to adapt,
667 compare and make the best use of the parallel imaging capabilities of the coil. The HCP-NHP analysis
668 pipelines are also available on github along with the HCP-Style macaque specific FIX training files
669 (<https://github.com/Washington-University/NHPPipelines>).

670

671 *Coil Design*

672 Our multichannel receive coil, fabricated to closely fit a large macaque head (Fig. 1A) will allow
673 routine imaging of macaque monkeys of different species with a range of lateral muscles and head
674 sizes. The close proximity of the coil to the head allows high SNR in the brain with further SNR gains
675 in the cortex produced by the small size of the elements (Fig. 1) (Janssens et al., 2013; Wiggins et al.,
676 2006). This design allowed acquisition of both T1w and T2w structural whole-brain image acquisition
677 with a 0.5mm isotropic resolution in 22 minutes (Fig. 3a, b). In conjunction with homogeneous RF
678 transmission (Fig. 3C, D), these two features enabled automatic and robust subcortical
679 segmentations and reconstructions of pial and white matter surfaces (Supplementary Fig. S4).

680

681 Twenty-four receive elements were arranged so as to optimize efficiency of spatial encoding capability
682 in the axial slice direction (Fig. 1B, D). This geometrical arrangement yields a relatively small noise
683 correlation coefficient (0.084), which is smaller than in previous macaque multi-channel coil designs
684 such as 0.12 in a 24-channel (Gilbert et al., 2016) and 0.22 in a 22-channel (Janssens et al., 2013). Our
685 coil design together with slice and in-plane accelerated imaging allowed up to five-fold and two-by-
686 two (MB-by-GRAPPA) accelerations for fMRI and dMRI, respectively. Moreover, this substantially
687 improved the imaging data quality through increased efficiency in accumulation of data volumes
688 (rfMRI: over 8000 volumes; and dMRI: 500 diffusion directions, all acquired in a single session in a

689 period of 140 minutes). Taken together, our 24-channel coil highlights the benefit of accelerated
690 imaging achieved through the geometrical arrangement and low noise correlation of the coil elements.

691

692 *Resting-state fMRI*

693 To accurately map BOLD signals onto the cortical sheet, the image resolution (1.25 mm isotropic)
694 was matched with 5th percentile of cortical thickness (Fig. 4N, O, P) to reduce the partial volume
695 effects from white matter and CSF signals (Glasser et al., 2013), following the HCP data acquisition
696 strategy at 3T (resolution 2 mm, the 5th percentile of human cortical thickness (Glasser et al., 2013)).
697 The reduction from an isotropic volume of 2 mm to 1.25 mm, however, incurs a 4-fold SNR penalty.
698 Nonetheless, tSNR of fMRI in macaque (Fig. 3G, H) is superior to that in the HCP acquired with
699 comparable imaging parameters (Supplementary Fig. S3, Table S1). This tSNR gain may be primarily
700 attributed to the close proximity to the animal and small diameter of the receive coil elements, with
701 an additional gain from relatively small bandwidth. This illustrates the power of parallel imaging to
702 overcome a physical size difference of a factor of twelve (macaque and human brain volumes are
703 approximately 100 cm³ and 1200 cm³, respectively).

704

705 While informative, tSNR is not an explicit measure of fMRI sensitivity to blood flow changes induced
706 by neural activity. It is well known that variation of fMRI signal is a mixture of nuisance (e.g. motion
707 and respiration) and neural BOLD components. To obtain insight into the content of our fMRI signals,
708 we categorized different signal sources and found that neural BOLD signal explains approximately
709 4.1% of the total fMRI variance (in data grand mean scaled to 10,000; corresponding to 773 ± 438 in
710 absolute variance) in anesthetized macaque resting-state (Fig. 6). In HCP fMRI data (awake-state),
711 neural BOLD signal explains approximately 7.7% of total variance (corresponding to 4158 ± 1594 in
712 absolute variance (Glasser et al., 2018; Marcus et al., 2013)). Because the image acquisition
713 protocols and image qualities are similar across the studies (Supplementary Fig. S3), we speculate
714 that the lower BOLD neural signal in our macaque data may be due to, 1) attenuated thalamo-
715 cortical and cortico-cortical synchronization in the anesthetized state, and/or 2) a ceiling effect of
716 signals due to relatively high blood flow, oxygen extraction rate, and saturation in anesthetized
717 macaque brain (Kudomi et al., 2005). This issue may be overcome with widely used contrast agents
718 (i.e. MION) and cerebral blood volume weighted fMRI (Mandeville et al., 1998) to boost CNR.
719 Nonetheless, the relatively small contribution of neural BOLD signal to the total variance highlights
720 the critical importance of post-processing to clean up nuisance signals to obtain functional
721 connectivity estimates that are neurobiologically meaningful. ICA-based FIX denoising has been
722 established to be very successful at removing non-random time-varying spatially specific artefacts

723 (e.g. movement, vascular and cerebrospinal fluid pulsation or scanning artefacts) in the human
724 resting-state fMRI (Griffanti et al., 2017, 2014; Salimi-Khorshidi et al., 2014; Smith et al., 2013). Here,
725 we demonstrated that FIX is also very successful reducing such artefacts (6.0% of total variance, Fig.
726 6) with over 98% classification accuracy (threshold at 20, Table 1) in the macaque resting-state fMRI.
727 The relative global mean variance and its reduction in macaque (1.5% before cleanup and 1.0% after
728 cleanup) is smaller in comparison to the HCP (3.2% before cleanup and 2.2% after cleanup) (Glasser
729 et al., 2018). This smaller global signal variance in anesthetized macaques can be attributed to more
730 stable global blood flow because respirations and pCO₂ were regulated by mechanical ventilation
731 (Birn et al., 2006). The majority of the signal variance, however, is unstructured noise (>60%), in
732 particular at subcortical regions that are distant from the coil elements (Supplementary Fig. S6),
733 which can be effectively reduced using parcellation and/or Wishart filtering (Fig. 8B) (Glasser et al.,
734 2016b).

735

736 The advantages of our experimental methodology was further demonstrated by the capability to
737 identify an average (across sessions/animals) of 21 ± 9 signal (neural) components at 3T (Fig. 5, for
738 exemplar signal components see Fig. 5 in BALSAs). A previous report using group-ICA from six
739 anesthetized macaques at 7T identified 11 RSNs (Hutchison et al., 2011). Our preliminary results
740 replicate several of these RSNs. Taken together, from the data quality perspective, the 24-channel
741 coil yields macaque rfMRI data that can be accurately and sensitively mapped onto cortical sheet
742 and is comparable in quality with the HCP rfMRI data, whereas from the physiology perspective, we
743 must be cautious when making inferences because of the potential effects of anesthesia on both
744 neural activity and neurovascular coupling. We will explore this topic in future work on a specialized
745 coil for awake monkey imaging.

746

747 While scaling the fMRI resolution with respect to the cortical thickness is a minimum requirement to
748 accurately localize BOLD signal within the cortical sheet, another important factor is the size of
749 functional imaging voxels relative to the area of the cortical surface for identifying sharp gradient
750 ridges in FC (Glasser et al., 2016a). We found that macaque cortical grey matter surface area is
751 $\approx 10,100 \text{ mm}^2$ per hemisphere, which is close to previous estimates of $11,900 \text{ mm}^2$ (Chaplin et al.,
752 2013) and $9,600 \text{ mm}^2$ (Donahue et al., 2018). Given that one cortical hemisphere is expected to
753 contain 130-140 cortical areas (Van Essen et al., 2011), an average parcel corresponds to an
754 approximate area of 70 mm^2 or 70 greyordinates (in our standard 10k greyordinate per hemisphere
755 space for the macaque with 1.25mm average spacing between greyordinates). In comparison, each
756 human cortical hemisphere has an approximate area of $88,200 \text{ mm}^2$, about is 9-fold larger than in

757 macaque. Since it has 180 cortical areas (Glasser et al., 2016a), an average human cortical parcel
758 corresponds to an area of 490 mm² or ≈160 greyordinates (in the HCP standard 32k greyordinates
759 per hemisphere space for humans). This suggests that identifying clear gradient ridges in FC can be
760 more reliably assessed in the HCP in comparison to our macaque setup, which can be attributed to
761 higher number of greyordinates and 9-fold larger cortical area in humans than in macaques. Viewed
762 from another perspective, since macaque cortex contains 0.85 billion neurons per hemisphere
763 (Herculano-Houzel et al., 2007), a single greyordinate (in 10k space) samples about 85,000 neurons
764 on average. In comparison, since human cortex contain 8.2 billion neurons per hemisphere (Azevedo
765 et al., 2009), so a single HCP greyordinate (in 32k space) samples an average of 270,000 neurons,
766 about three-fold greater than in the macaque. Taken together, while the expected number of
767 greyordinates per cortical area is larger in the human (due to 9-fold larger cortical area of the human
768 brain), our HCP-style approach for the macaque samples fewer neurons per greyordinate (due to the
769 4-fold smaller voxel volume).

770

771 *Diffusion MRI*

772 Spatial resolution is among the most important factors for resolving crossing fiber architecture
773 (Donahue et al., 2016) and microstructural properties such as cortical radial anisotropy (Fan et al.,
774 2017; Sotiropoulos et al., 2016). The ratio between the voxel size and macaque white matter volume
775 for the presented dMRI protocol ($0.73 \text{ mm}^3 / 23.000 \text{ mm}^3 \approx 3 \times 10^{-5}$) approximately matches 2.5 mm
776 isotropic resolution in the human white matter ($16 \text{ mm}^3 / 500.000 \text{ mm}^3 \approx 3 \times 10^{-5}$) but is an order of
777 magnitude larger than in the HCP ($1.95 \text{ mm}^3 / 500.000 \text{ mm}^3 \approx 4 \times 10^{-6}$), although a more precise
778 comparison would require investigations on features such as radii of curvature, tract and blade
779 thickness. Smaller voxel size could aid in distinguishing challenging fiber pathways, however, under
780 our experimental conditions further reduction was impractical due to gradient power and SNR
781 limitations.

782

783 To mitigate this limitation, our strategy was to acquire data with exceptionally high angular
784 resolution (500 directions) capitalizing on two-by-two acceleration (out-of-plane MB and in-plane
785 GRAPPA) enabled by the multichannel array coil. The effect of this strategy was shown in the
786 comparable sensitivity to 3rd crossing fibers between species (Fig. 8), despite the resolution
787 limitation in macaque. A recent ex vivo macaque study used high-quality, high-field magnetic field
788 (4.7T), long data acquisition (≈27 h) postmortem and gadolinium enhanced diffusion scans to
789 demonstrate a relatively good correspondence between probabilistic tractography and quantitative
790 retrograde tracer (R=0.55-0.60) (Donahue et al., 2016). Here, we replicated a part of those results

791 (Fig. 8E, F), thus, augmenting the findings of Donahue and colleagues to *in vivo* applications that are
792 within practical time limitations (≈ 30 min). Taken together, these results suggest that the ‘HCP’-style
793 dMRI data acquisition protocols are well positioned to produce quantitative tractography measures
794 that are neuroanatomically meaningful.

795

796 The high spatial resolution with respect to cortical thickness enabled us to carry out cortical surface
797 mapping of neurite properties and to provide preliminary evidence for nonuniformity in the
798 composition and distribution of neurites in macaque cerebral cortex (Fig. 9C, D). Neurite properties
799 are considered important because the density of neurites constitute basic building units (axons and
800 dendrites) of neuronal networks, while ODI provides an indicator of the heterogeneity of neurite
801 fiber orientations, a ratio between tangential and radial fibers (Fukutomi et al., 2018). We found that
802 NDI was highest in V1 and higher than average in other visual representation areas (V2, V3, V4, and
803 MT), somatosensory (1, 2, 3 and A1), motor (M1) and granular prefrontal (Fig. 9C), cortical
804 distributions resembled those of myelin contrast (Fig. 4L). ODI was high in early somatosensory,
805 auditory and visual cortices (Fig. 9D). Together, these results are in good agreement with the HCP
806 data (Fukutomi et al., 2018).

807

808 *Towards Improved Macaque Connectomes and Cross-species Connectome Comparisons*

809 The construction of a high-quality connectome requires anatomically accurate definitions of parcels
810 that represent a biologically meaningful partition of brain areas based on their function,
811 architecture, connectivity, and topography (Felleman and Van Essen, 1991; Glasser et al., 2016a; Van
812 Essen and Glasser, 2018). Comparison between transitions in multimodal neuroimaging contrasts,
813 such as MT myelination (Fig. 4C) and functional connectivity (Fig. 8A, E), are particularly suggestive
814 of brain area boundaries (Glasser et al., 2016a). Therefore, the approach to data collection and
815 analysis presented here provides macaque data that may aid in multi-modal parcellation of the
816 macaque and generation of structural and functional connectomes (Glasser et al., 2016b), though a
817 robust delineation of cortical areas into functionally distinct areas will assuredly require analysis of a
818 more extensive dataset.

819

820 These HCP-style macaque data also provide an attractive substrate for multi-modal registration
821 across species—in particular, macaques and humans. Just as myelin maps and resting state networks
822 are used to register across human subjects (Robinson et al., 2018, 2014), they could be used to
823 register the cerebral cortex between group averages of humans and macaques. This would allow
824 direct comparisons between human and macaque structural and functional connectivity (Mars et al.,

825 2018b). That said, we expect that the gains for cross-individual registration with areal features in the
826 macaque will be less than those in humans simply because folding patterns and the relationships
827 between folds and areas are less variable in macaques than they are in humans. Additionally, this
828 approach to macaque imaging acquisition and analysis can be used to form structural and functional
829 connectomes in the macaque for comparison with invasively measured tracer datasets (Donahue et
830 al., 2016; Glasser et al., 2016b). Such validation analyses will help to determine the optimal methods
831 for forming structural and functional connectomes in human studies (Jbabdi et al., 2013), where a
832 direct comparison with a gold standard is not available. Future work will also explore cross-species
833 comparisons between macaques and marmosets imaged using specialized hardware and an HCP-
834 style approach. These acquisition and analysis methods can also be applied to study disease models
835 in primate species where controlled and invasive methods can be used to investigate causality and
836 plasticity of structural and functional connectomes and their importance in shaping primate
837 behavior.

838

839 *Conclusions*

840 A 24-channel phased-array coil for 3T was constructed and optimized for in vivo parallel imaging of
841 macaque monkey brain. The coil provided high SNR whole-brain coverage and allowed parallel
842 imaging with high speed acquisition by a five-fold and four-fold increase in functional and diffusion
843 MRI, respectively. The data acquisition strategy in combination with the HCP-NHP minimal
844 preprocessing pipelines enabled robust mapping of structural and functional properties onto surface
845 of the cortex. The presented protocols can be acquired within a single imaging session and represent
846 compelling advance in identifying multi-modal cortical topology and structural and functional
847 connectomes in the macaque. Overall, this study demonstrates that MRI studies in animals may
848 benefit from adapting the methodologies introduced by the HCP.

849

850 **Notes**

851 Data of figures and supplementary figures are available at <https://balsa.wustl.edu/study/show/LPDP>
852 Supplementary Information is available in the online version of the paper.

853

854 **Acknowledgements**

855 We thank Henry Kennedy for his helpful comments, and Stephen Frey, Nobuyoshi Tanki, Chiho
856 Takeda, Akihiro Kawasaki, Reiko Kobayashi, Kenji Mitsui and Hanako Hirose for their technical help.
857 This research is partially supported by the program for Brain/MINDS and Brain/MINDS-beyond from
858 Japan Agency for Medical Research and development, AMED (JP18dm0207001, JP18dm0307006), by

859 RIKEN Compass to Healthy Life Research Complex Program from Japan Science and Technology
860 Agency, JST, by MEXT KAKENHI Grant (16H03300, 16H03306, 16H01626, 15K12779 to T.H. and
861 JP26640065, JP16H06531 to Y.G.), NIH F30 MH097312 (M.F.G.) and RO1 MH-60974 (D.C.V.E.) and by
862 the National Institutes of Natural Sciences (NINS) program for cross-disciplinary study (2013-2015)
863 (Y.G.) and by Wellcome Trust (SMS, JS). The author Yoshihiko Kawabata holds financial conflict of
864 interest because the coil is produced by his company (Takashima Seisakusho Co. Ltd., Tokyo, Japan)
865 and distributed through his collaboration company (Rogue Research, Montreal, Canada). The other
866 authors have no conflicts of interest to declare.

867

868 **Author Contributions**

869 T.H., and M.F.G. designed the study.

870 J.A.A, Y.H., M.F.G. and T.H. analyzed data.

871 M.F.G., C.J.D., and T.H. developed new software tools.

872 J.A.A, T. O., M. O. Y. K, Y.U, K.M, K. N., M.Y, A.Y., Y.G. and T.H. performed experiments.

873 J.A.A, M.B., M.F.G, T.S.C, S.J., S.N.S, S.S, D.C.V.E and T.H. wrote the paper.

874

875 **References**

876

877 Andersson, J.L.R., Skare, S., Ashburner, J., 2003. How to correct susceptibility distortions in spin-echo
878 echo-planar images: application to diffusion tensor imaging. *NeuroImage* 20, 870–888.

879 [https://doi.org/10.1016/S1053-8119\(03\)00336-7](https://doi.org/10.1016/S1053-8119(03)00336-7)

880 Andersson, J.L.R., Sotiropoulos, S.N., 2016. An integrated approach to correction for off-resonance
881 effects and subject movement in diffusion MR imaging. *NeuroImage* 125, 1063–1078.

882 Andersson, J.L.R., Sotiropoulos, S.N., 2015. Non-parametric representation and prediction of single-
883 and multi-shell diffusion-weighted MRI data using Gaussian processes. *NeuroImage* 122,
884 166–176. <https://doi.org/10.1016/j.neuroimage.2015.07.067>

885 Azevedo, F.A.C., Carvalho, L.R.B., Grinberg, L.T., Farfel, J.M., Ferretti, R.E.L., Leite, R.E.P., Filho, W.J.,
886 Lent, R., Herculano-Houzel, S., 2009. Equal numbers of neuronal and nonneuronal cells make
887 the human brain an isometrically scaled-up primate brain. *J. Comp. Neurol.* 513, 532–541.
888 <https://doi.org/10.1002/cne.21974>

889 Bastiani, M., Cottaar, M., Fitzgibbon, S.P., Suri, S., Alfaro-Almagro, F., Sotiropoulos, S.N., Jbabdi, S.,
890 Andersson, J.L.R., 2019. Automated quality control for within and between studies diffusion
891 MRI data using a non-parametric framework for movement and distortion correction.
892 *NeuroImage* 184, 801–812. <https://doi.org/10.1016/j.neuroimage.2018.09.073>

893 Behrens, T.E.J., Berg, H.J., Jbabdi, S., Rushworth, M.F.S., Woolrich, M.W., 2007. Probabilistic diffusion
894 tractography with multiple fibre orientations: What can we gain? *NeuroImage* 34, 144–155.
895 <https://doi.org/10.1016/j.neuroimage.2006.09.018>

896 Birn, R.M., Diamond, J.B., Smith, M.A., Bandettini, P.A., 2006. Separating respiratory-variation-
897 related fluctuations from neuronal-activity-related fluctuations in fMRI. *NeuroImage* 31,
898 1536–1548. <https://doi.org/10.1016/j.neuroimage.2006.02.048>

899 Brodmann K., 1905. Beitrage zur histologischen localisation der grosshirnrinde. Dritte Mitteilung. Die
900 Rinden-felder der niederen Affen. *J Psychol Neurol* 177–226.

901 Chaplin, T.A., Yu, H.-H., Soares, J.G.M., Gattass, R., Rosa, M.G.P., 2013. A Conserved Pattern of
902 Differential Expansion of Cortical Areas in Simian Primates. *J. Neurosci.* 33, 15120–15125.
903 <https://doi.org/10.1523/JNEUROSCI.2909-13.2013>

904 Coalson, T.S., Van Essen, D.C., Glasser, M., 2018. Lost in Space: The Impact of Traditional
905 Neuroimaging Methods on the Spatial Localization of Cortical Areas.
906 <https://doi.org/10.1101/255620>

907 Donahue, C.J., Glasser, M.F., Preuss, T.M., Rilling, J.K., Essen, D.C.V., 2018. Quantitative assessment
908 of prefrontal cortex in humans relative to nonhuman primates. *Proc. Natl. Acad. Sci.*
909 201721653. <https://doi.org/10.1073/pnas.1721653115>

910 Donahue, C.J., Sotiropoulos, S.N., Jbabdi, S., Hernandez-Fernandez, M., Behrens, T.E., Dyrby, T.B.,
911 Coalson, T., Kennedy, H., Knoblauch, K., Essen, D.C.V., Glasser, M.F., 2016. Using Diffusion
912 Tractography to Predict Cortical Connection Strength and Distance: A Quantitative
913 Comparison with Tracers in the Monkey. *J. Neurosci.* 36, 6758–6770.
914 <https://doi.org/10.1523/JNEUROSCI.0493-16.2016>

915 Fan, Q., Nummenmaa, A., Polimeni, J.R., Witzel, T., Huang, S.Y., Wedeen, V.J., Rosen, B.R., Wald, L.L.,
916 2017. High b-value and high Resolution Integrated Diffusion (HIBRID) imaging. *NeuroImage*
917 150, 162–176. <https://doi.org/10.1016/j.neuroimage.2017.02.002>

918 Felleman, D.J., Van Essen, D., 1991. Distributed hierarchical processing in the primate cerebral
919 cortex. *Cereb. Cortex N. Y. N* 1991 1, 1–47. <https://doi.org/10.1093/cercor/1.1.1>

920 Fischl, B., 2012. FreeSurfer. *NeuroImage, 20 YEARS OF fMRI* 20 YEARS OF fMRI 62, 774–781.
921 <https://doi.org/10.1016/j.neuroimage.2012.01.021>

922 Fischl, B., Salat, D.H., Busa, E., Albert, M., Dieterich, M., Haselgrove, C., van der Kouwe, A., Killiany,
923 R., Kennedy, D., Klaveness, S., Montillo, A., Makris, N., Rosen, B., Dale, A.M., 2002. Whole
924 brain segmentation: automated labeling of neuroanatomical structures in the human brain.
925 *Neuron* 33, 341–355.

- 926 Fukutomi, H., Glasser, M.F., Zhang, H., Autio, J.A., Coalson, T.S., Okada, T., Togashi, K., Van Essen,
927 D.C., Hayashi, T., 2018. Neurite imaging reveals microstructural variations in human cerebral
928 cortical gray matter. *NeuroImage*. <https://doi.org/10.1016/j.neuroimage.2018.02.017>
- 929 Gilbert, K.M., Gati, J.S., Barker, K., Everling, S., Menon, R.S., 2016. Optimized parallel transmit and
930 receive radiofrequency coil for ultrahigh-field MRI of monkeys. *NeuroImage* 125, 153–161.
931 <https://doi.org/10.1016/j.neuroimage.2015.10.048>
- 932 Glasser, M.F., Coalson, T.S., Bijsterbosch, J.D., Harrison, S.J., Harms, M.P., Anticevic, A., Essen, D.C.V.,
933 Smith, S.M., 2017. Using Temporal ICA to Selectively Remove Global Noise While Preserving
934 Global Signal in Functional MRI Data. *bioRxiv* 193862. <https://doi.org/10.1101/193862>
- 935 Glasser, M.F., Coalson, T.S., Bijsterbosch, J.D., Harrison, S.J., Harms, M.P., Anticevic, A., Van Essen,
936 D.C., Smith, S.M., 2018. Using temporal ICA to selectively remove global noise while
937 preserving global signal in functional MRI data. *NeuroImage* 181, 692–717.
938 <https://doi.org/10.1016/j.neuroimage.2018.04.076>
- 939 Glasser, M.F., Coalson, T.S., Robinson, E.C., Hacker, C.D., Harwell, J., Yacoub, E., Ugurbil, K.,
940 Andersson, J., Beckmann, C.F., Jenkinson, M., Smith, S.M., Van Essen, D.C., 2016a. A multi-
941 modal parcellation of human cerebral cortex. *Nature* 536, 171–178.
942 <https://doi.org/10.1038/nature18933>
- 943 Glasser, M.F., Goyal, M.S., Preuss, T.M., Raichle, M.E., Van Essen, D.C., 2014. Trends and properties
944 of human cerebral cortex: Correlations with cortical myelin content. *NeuroImage, In-vivo*
945 *Brodman Mapping of the Human Brain* 93, Part 2, 165–175.
946 <https://doi.org/10.1016/j.neuroimage.2013.03.060>
- 947 Glasser, M.F., Smith, S.M., Marcus, D.S., Andersson, J.L.R., Auerbach, E.J., Behrens, T.E.J., Coalson,
948 T.S., Harms, M.P., Jenkinson, M., Moeller, S., Robinson, E.C., Sotiropoulos, S.N., Xu, J.,
949 Yacoub, E., Ugurbil, K., Essen, D.C.V., 2016b. The Human Connectome Project’s
950 neuroimaging approach. *Nat. Neurosci.* 19, 1175–1187. <https://doi.org/10.1038/nn.4361>
- 951 Glasser, M.F., Sotiropoulos, S.N., Wilson, J.A., Coalson, T.S., Fischl, B., Andersson, J.L., Xu, J., Jbabdi,
952 S., Webster, M., Polimeni, J.R., Van Essen, D.C., Jenkinson, M., 2013. The minimal
953 preprocessing pipelines for the Human Connectome Project. *NeuroImage* 80, 105–124.
954 <https://doi.org/10.1016/j.neuroimage.2013.04.127>
- 955 Glasser, M.F., Van Essen, D.C., 2011. Mapping Human Cortical Areas In Vivo Based on Myelin
956 Content as Revealed by T1- and T2-Weighted MRI. *J. Neurosci.* 31, 11597–11616.
957 <https://doi.org/10.1523/JNEUROSCI.2180-11.2011>
- 958 Goense, J.B.M., Logothetis, N.K., 2008. Neurophysiology of the BOLD fMRI Signal in Awake Monkeys.
959 *Curr. Biol.* 18, 631–640. <https://doi.org/10.1016/j.cub.2008.03.054>
- 960 Gomori, J.M., Holland, G.A., Grossman, R.I., Geftter, W.B., Lenkinski, R.E., 1988. Fat suppression by
961 section-select gradient reversal on spin-echo MR imaging. *Work in progress. Radiology* 168,
962 493–495. <https://doi.org/10.1148/radiology.168.2.3393670>
- 963 Gonzalez-Castillo, J., Duthie, K.N., Saad, Z.S., Chu, C., Bandettini, P.A., Luh, W.-M., 2013. Effects of
964 image contrast on functional MRI image registration. *NeuroImage* 67, 163–174.
965 <https://doi.org/10.1016/j.neuroimage.2012.10.076>
- 966 Greve, D.N., Fischl, B., 2009. Accurate and robust brain image alignment using boundary-based
967 registration. *NeuroImage* 48, 63–72. <https://doi.org/10.1016/j.neuroimage.2009.06.060>
- 968 Griffanti, L., Douaud, G., Bijsterbosch, J., Evangelisti, S., Alfaro-Almagro, F., Glasser, M.F., Duff, E.P.,
969 Fitzgibbon, S., Westphal, R., Carone, D., Beckmann, C.F., Smith, S.M., 2017. Hand
970 classification of fMRI ICA noise components. *NeuroImage, Cleaning up the fMRI time series:*
971 *Mitigating noise with advanced acquisition and correction strategies* 154, 188–205.
972 <https://doi.org/10.1016/j.neuroimage.2016.12.036>
- 973 Griffanti, L., Salimi-Khorshidi, G., Beckmann, C.F., Auerbach, E.J., Douaud, G., Sexton, C.E., Zsoldos,
974 E., Ebmeier, K.P., Filippini, N., Mackay, C.E., Moeller, S., Xu, J., Yacoub, E., Baselli, G., Ugurbil,
975 K., Miller, K.L., Smith, S.M., 2014. ICA-based artefact removal and accelerated fMRI

- 976 acquisition for improved resting state network imaging. *NeuroImage* 95, 232–247.
977 <https://doi.org/10.1016/j.neuroimage.2014.03.034>
- 978 Griswold, M.A., Jakob, P.M., Heidemann, R.M., Nittka, M., Jellus, V., Wang, J., Kiefer, B., Haase, A.,
979 2002. Generalized autocalibrating partially parallel acquisitions (GRAPPA). *Magn. Reson.*
980 *Med.* 47, 1202–1210. <https://doi.org/10.1002/mrm.10171>
- 981 Helms, G., Garea-Rodriguez, E., Schlumbohm, C., König, J., Dechent, P., Fuchs, E., Wilke, M., 2013.
982 Structural and quantitative neuroimaging of the common marmoset monkey using a clinical
983 MRI system. *J. Neurosci. Methods* 215, 121–131.
984 <https://doi.org/10.1016/j.jneumeth.2013.02.011>
- 985 Herculano-Houzel, S., Collins, C.E., Wong, P., Kaas, J.H., 2007. Cellular scaling rules for primate
986 brains. *Proc. Natl. Acad. Sci.* 104, 3562–3567. <https://doi.org/10.1073/pnas.0611396104>
- 987 Hernández, M., Guerrero, G.D., Cecilia, J.M., García, J.M., Inuggi, A., Jbabdi, S., Behrens, T.E.J.,
988 Sotiropoulos, S.N., 2013. Accelerating Fibre Orientation Estimation from Diffusion Weighted
989 Magnetic Resonance Imaging Using GPUs. *PLOS ONE* 8, e61892.
990 <https://doi.org/10.1371/journal.pone.0061892>
- 991 Hernandez-Fernandez, M., Reguly, I., Jbabdi, S., Giles, M., Smith, S., Sotiropoulos, S.N., 2018. Using
992 GPUs to accelerate computational diffusion MRI: From microstructure estimation to
993 tractography and connectomes. *NeuroImage* 188, 598–615.
994 <https://doi.org/10.1016/j.neuroimage.2018.12.015>
- 995 Hutchison, R.M., Leung, L.S., Mirsattari, S.M., Gati, J.S., Menon, R.S., Everling, S., 2011. Resting-state
996 networks in the macaque at 7 T. *NeuroImage* 56, 1546–1555.
997 <https://doi.org/10.1016/j.neuroimage.2011.02.063>
- 998 Janssens, T., Keil, B., Serano, P., Mareyam, A., McNab, J.A., Wald, L.L., Vanduffel, W., 2013. A 22-
999 channel receive array with Helmholtz transmit coil for anesthetized macaque MRI at 3 T.
1000 *NMR Biomed.* 26, 1431–1440. <https://doi.org/10.1002/nbm.2970>
- 1001 Jbabdi, S., Lehman, J.F., Haber, S.N., Behrens, T.E., 2013. Human and monkey ventral prefrontal
1002 fibers use the same organizational principles to reach their targets: tracing versus
1003 tractography. *J. Neurosci. Off. J. Soc. Neurosci.* 33, 3190–3201.
1004 <https://doi.org/10.1523/JNEUROSCI.2457-12.2013>
- 1005 Jbabdi, S., Sotiropoulos, S.N., Savio, A.M., Graña, M., Behrens, T.E.J., 2012. Model-based analysis of
1006 multishell diffusion MR data for tractography: how to get over fitting problems. *Magn.*
1007 *Reson. Med.* 68, 1846–1855. <https://doi.org/10.1002/mrm.24204>
- 1008 Jenkinson, M., Bannister, P., Brady, M., Smith, S., 2002. Improved Optimization for the Robust and
1009 Accurate Linear Registration and Motion Correction of Brain Images. *NeuroImage* 17, 825–
1010 841. <https://doi.org/10.1006/nimg.2002.1132>
- 1011 Khachaturian, M.H., 2010. A 4-channel 3 Tesla phased array receive coil for awake rhesus monkey
1012 fMRI and diffusion MRI experiments. *J. Biomed. Sci. Eng.* 3, 1085–1092.
1013 <https://doi.org/10.4236/jbise.2010.311141>
- 1014 Kudomi, N., Hayashi, T., Teramoto, N., Watabe, H., Kawachi, N., Ohta, Y., Kim, K.M., Iida, H., 2005.
1015 Rapid quantitative measurement of CMRO(2) and CBF by dual administration of (15)O-
1016 labeled oxygen and water during a single PET scan—a validation study and error analysis in
1017 anesthetized monkeys. *J Cereb Blood Flow Metab* 25, 1209–24.
- 1018 Mandeville, J.B., Marota, J.J.A., Kosofsky, B.E., Keltner, J.R., Weissleder, R., Rosen, B.R., Weisskoff,
1019 R.M., 1998. Dynamic functional imaging of relative cerebral blood volume during rat
1020 forepaw stimulation. *Magn. Reson. Med.* 39, 615–624.
1021 <https://doi.org/10.1002/mrm.1910390415>
- 1022 Marcus, D.S., Harms, M.P., Snyder, A.Z., Jenkinson, M., Wilson, J.A., Glasser, M.F., Barch, D.M.,
1023 Archie, K.A., Burgess, G.C., Ramaratnam, M., Hodge, M., Horton, W., Herrick, R., Olsen, T.,
1024 McKay, M., House, M., Hileman, M., Reid, E., Harwell, J., Coalson, T., Schindler, J., Elam, J.S.,
1025 Curtiss, S.W., Van Essen, D.C., 2013. Human Connectome Project informatics: Quality

- 1026 control, database services, and data visualization. *NeuroImage* 80, 202–219.
1027 <https://doi.org/10.1016/j.neuroimage.2013.05.077>
- 1028 Mareyam, A., Blau, J., Polimeni, J., Keil, B., Farivar, R., Benner, T., Vanduffel, W., Wald, L.L., 1823.
1029 Eight-channel array coil optimized for functional imaging of awake monkeys at 7T, in: *Proc.*
1030 *Intl. Soc. Mag. Reson. Med.* p. 2011.
- 1031 Markov, N.T., Ercsey-Ravasz, M.M., Gomes, R., R, A., Lamy, C., Magrou, L., Vezoli, J., Misery, P.,
1032 Falchier, A., Quilodran, R., Gariel, M.A., Sallet, J., Gamanut, R., Huissoud, C., Clavagnier, S.,
1033 Giroud, P., Sappey-Mariniere, D., Barone, P., Dehay, C., Toroczkai, Z., Knoblauch, K., Essen, V.,
1034 C, D., Kennedy, H., 2014. A Weighted and Directed Interareal Connectivity Matrix for
1035 Macaque Cerebral Cortex. *Cereb. Cortex* 24, 17–36. <https://doi.org/10.1093/cercor/bhs270>
- 1036 Mars, R.B., Passingham, R.E., Jbabdi, S., 2018a. Connectivity Fingerprints: From Areal Descriptions to
1037 Abstract Spaces. *Trends Cogn. Sci.* 22, 1026–1037.
1038 <https://doi.org/10.1016/j.tics.2018.08.009>
- 1039 Mars, R.B., Sotiropoulos, S.N., Passingham, R.E., Sallet, J., Verhagen, L., Khrapitchev, A.A., Sibson, N.,
1040 Jbabdi, S., 2018b. Whole brain comparative anatomy using connectivity blueprints. *eLife* 7.
1041 <https://doi.org/10.7554/eLife.35237>
- 1042 McKeown, M.J., Makeig, S., Brown, G.G., Jung, T.P., Kindermann, S.S., Bell, A.J., Sejnowski, T.J., 1998.
1043 Analysis of fMRI data by blind separation into independent spatial components. *Hum. Brain*
1044 *Mapp.* 6, 160–188.
- 1045 Mesulam, M.-M., Mufson, E.J., 1982. Insula of the old world monkey. III: Efferent cortical output and
1046 comments on function. *J. Comp. Neurol.* 212, 38–52.
1047 <https://doi.org/10.1002/cne.902120104>
- 1048 Moeller, S., Yacoub, E., Olman, C.A., Auerbach, E., Strupp, J., Harel, N., Uğurbil, K., 2010. Multiband
1049 multislice GE-EPI at 7 tesla, with 16-fold acceleration using partial parallel imaging with
1050 application to high spatial and temporal whole-brain fMRI. *Magn. Reson. Med.* 63, 1144–
1051 1153. <https://doi.org/10.1002/mrm.22361>
- 1052 Mugler, J.P., Bao, S., Mulkern, R.V., Guttman, C.R.G., Robertson, R.L., Jolesz, F.A., Brookeman, J.R.,
1053 2000. Optimized Single-Slab Three-dimensional Spin-Echo MR Imaging of the Brain.
1054 *Radiology* 216, 891–899. <https://doi.org/10.1148/radiology.216.3.r00au46891>
- 1055 Mugler, J.P., Brookeman, J.R., 1990. Three-dimensional magnetization-prepared rapid gradient-echo
1056 imaging (3D MP RAGE). *Magn. Reson. Med.* 15, 152–157.
1057 <https://doi.org/10.1002/mrm.1910150117>
- 1058 Passingham, R., 2009. How good is the macaque monkey model of the human brain? *Curr. Opin.*
1059 *Neurobiol., Cognitive neuroscience* 19, 6–11. <https://doi.org/10.1016/j.conb.2009.01.002>
- 1060 Power, J.D., 2016. A simple but useful way to assess fMRI scan qualities. *NeuroImage*.
1061 Power, J.D., Mitra, A., Laumann, T.O., Snyder, A.Z., Schlaggar, B.L., Petersen, S.E., 2014. Methods to
1062 detect, characterize, and remove motion artifact in resting state fMRI. *NeuroImage* 84, 320–
1063 341. <https://doi.org/10.1016/j.neuroimage.2013.08.048>
- 1064 Rilling, J.K., Glasser, M.F., Preuss, T.M., Ma, X., Zhao, T., Hu, X., Behrens, T.E.J., 2008. The evolution
1065 of the arcuate fasciculus revealed with comparative DTI. *Nat. Neurosci.* 11, 426–428.
1066 <https://doi.org/10.1038/nn2072>
- 1067 Robinson, E.C., Garcia, K., Glasser, M.F., Chen, Z., Coalson, T.S., Makropoulos, A., Bozek, J., Wright,
1068 R., Schuh, A., Webster, M., Hutter, J., Price, A., Cordero Grande, L., Hughes, E., Tusor, N.,
1069 Bayly, P.V., Van Essen, D.C., Smith, S.M., Edwards, A.D., Hajnal, J., Jenkinson, M., Glocker, B.,
1070 Rueckert, D., 2018. Multimodal surface matching with higher-order smoothness constraints.
1071 *NeuroImage* 167, 453–465. <https://doi.org/10.1016/j.neuroimage.2017.10.037>
- 1072 Robinson, E.C., Jbabdi, S., Glasser, M.F., Andersson, J., Burgess, G.C., Harms, M.P., Smith, S.M., Van
1073 Essen, D.C., Jenkinson, M., 2014. MSM: A new flexible framework for Multimodal Surface
1074 Matching. *NeuroImage* 100, 414–426. <https://doi.org/10.1016/j.neuroimage.2014.05.069>
- 1075 Roemer, P.B., Edelstein, W.A., Hayes, C.E., Souza, S.P., Mueller, O.M., 1990. The NMR phased array.
1076 *Magn. Reson. Med.* 16, 192–225. <https://doi.org/10.1002/mrm.1910160203>

- 1077 Salimi-Khorshidi, G., Douaud, G., Beckmann, C.F., Glasser, M.F., Griffanti, L., Smith, S.M., 2014.
1078 Automatic denoising of functional MRI data: Combining independent component analysis
1079 and hierarchical fusion of classifiers. *NeuroImage* 90, 449–468.
1080 <https://doi.org/10.1016/j.neuroimage.2013.11.046>
- 1081 Setsompop, K., Cohen-Adad, J., Gagoski, B.A., Raij, T., Yendiki, A., Keil, B., Wedeen, V.J., Wald, L.L.,
1082 2012. Improving diffusion MRI using simultaneous multi-slice echo planar imaging.
1083 *NeuroImage* 63, 569–580. <https://doi.org/10.1016/j.neuroimage.2012.06.033>
- 1084 Smith, R.E., Tournier, J.-D., Calamante, F., Connelly, A., 2012. Anatomically-constrained tractography:
1085 improved diffusion MRI streamlines tractography through effective use of anatomical
1086 information. *NeuroImage* 62, 1924–1938.
1087 <https://doi.org/10.1016/j.neuroimage.2012.06.005>
- 1088 Smith, S.M., Beckmann, C.F., Andersson, J., Auerbach, E.J., Bijsterbosch, J., Douaud, G., Duff, E.,
1089 Feinberg, D.A., Griffanti, L., Harms, M.P., others, 2013. Resting-state fMRI in the human
1090 connectome project. *Neuroimage* 80, 144–168.
- 1091 Sotiropoulos, S.N., Hernández-Fernández, M., Vu, A.T., Andersson, J.L., Moeller, S., Yacoub, E.,
1092 Lenglet, C., Ugurbil, K., Behrens, T.E.J., Jbabdi, S., 2016. Fusion in diffusion MRI for improved
1093 fibre orientation estimation: An application to the 3T and 7T data of the Human Connectome
1094 Project. *NeuroImage* 134, 396–409. <https://doi.org/10.1016/j.neuroimage.2016.04.014>
- 1095 Sotiropoulos, S.N., Jbabdi, S., Xu, J., Andersson, J.L., Moeller, S., Auerbach, E.J., Glasser, M.F.,
1096 Hernandez, M., Sapiro, G., Jenkinson, M., Feinberg, D.A., Yacoub, E., Lenglet, C., Van Essen,
1097 D.C., Ugurbil, K., Behrens, T.E.J., 2013. Advances in diffusion MRI acquisition and processing
1098 in the Human Connectome Project. *NeuroImage* 80, 125–143.
1099 <https://doi.org/10.1016/j.neuroimage.2013.05.057>
- 1100 Stejskal, E.O., Tanner, J.E., 1965. Spin Diffusion Measurements: Spin Echoes in the Presence of a
1101 Time-Dependent Field Gradient. *J. Chem. Phys.* 42, 288. <https://doi.org/10.1063/1.1695690>
- 1102 Ugurbil, K., Xu, J., Auerbach, E.J., Moeller, S., Vu, A.T., Duarte-Carvajalino, J.M., Lenglet, C., Wu, X.,
1103 Schmitter, S., Van de Moortele, P.F., Strupp, J., Sapiro, G., De Martino, F., Wang, D., Harel,
1104 N., Garwood, M., Chen, L., Feinberg, D.A., Smith, S.M., Miller, K.L., Sotiropoulos, S.N., Jbabdi,
1105 S., Andersson, J.L.R., Behrens, T.E.J., Glasser, M.F., Van Essen, D.C., Yacoub, E., 2013. Pushing
1106 spatial and temporal resolution for functional and diffusion MRI in the Human Connectome
1107 Project. *NeuroImage, Mapping the Connectome* 80, 80–104.
1108 <https://doi.org/10.1016/j.neuroimage.2013.05.012>
- 1109 Van de Moortele, P.-F., Auerbach, E.J., Olman, C., Yacoub, E., Ugurbil, K., Moeller, S., 2009. T1
1110 weighted Brain Images at 7 Tesla Unbiased for Proton Density, T2* contrast and RF Coil
1111 Receive B1 Sensitivity with Simultaneous Vessel Visualization. *NeuroImage* 46, 432–446.
1112 <https://doi.org/10.1016/j.neuroimage.2009.02.009>
- 1113 Van Essen, D.C., Dierker, D.L., 2007. Surface-Based and Probabilistic Atlases of Primate Cerebral
1114 Cortex. *Neuron* 56, 209–225. <https://doi.org/10.1016/j.neuron.2007.10.015>
- 1115 Van Essen, D.C., Glasser, M.F., Dierker, D.L., Harwell, J., 2011. Cortical Parcellations of the Macaque
1116 Monkey Analyzed on Surface-Based Atlases. *Cereb. Cortex* bhr290.
1117 <https://doi.org/10.1093/cercor/bhr290>
- 1118 Van Essen, D.C., Glasser, M.F., 2018. Parcellating Cerebral Cortex: How Invasive Animal Studies
1119 Inform Noninvasive Mapmaking in Humans. *Neuron* 99, 640–663.
1120 <https://doi.org/10.1016/j.neuron.2018.07.002>
- 1121 Van Essen, D.C., Lewis, J.W., Drury, H.A., Hadjikhani, N., Tootell, R.B., Bakircioglu, M., Miller, M.I.,
1122 2001. Mapping visual cortex in monkeys and humans using surface-based atlases. *Vision Res.*
1123 41, 1359–1378. [https://doi.org/10.1016/S0042-6989\(01\)00045-1](https://doi.org/10.1016/S0042-6989(01)00045-1)
- 1124 Van Essen, D.C., Smith, J., Glasser, M.F., Elam, J., Donahue, C.J., Dierker, D.L., Reid, E.K., Coalson, T.,
1125 Harwell, J., 2017. The Brain Analysis Library of Spatial maps and Atlases (BALSA) database.
1126 *NeuroImage, Data Sharing Part II* 144, 270–274.
1127 <https://doi.org/10.1016/j.neuroimage.2016.04.002>

- 1128 Wang, L., Saalman, Y.B., Pinski, M.A., Arcaro, M.J., Kastner, S., 2012. Electrophysiological Low-
1129 Frequency Coherence and Cross-Frequency Coupling Contribute to BOLD Connectivity.
1130 *Neuron* 76, 1010–1020. <https://doi.org/10.1016/j.neuron.2012.09.033>
- 1131 Wiggins, G. c., Triantafyllou, C., Potthast, A., Reykowski, A., Nittka, M., Wald, L. I., 2006. 32-channel 3
1132 Tesla receive-only phased-array head coil with soccer-ball element geometry. *Magn. Reson.*
1133 *Med.* 56, 216–223. <https://doi.org/10.1002/mrm.20925>
- 1134 Wiggins, G.C., Polimeni, J.R., Potthast, A., Schmitt, M., Alagappan, V., Wald, L.L., 2009. 96-Channel
1135 receive-only head coil for 3 Tesla: design optimization and evaluation. *Magn. Reson. Med.*
1136 *Off. J. Soc. Magn. Reson. Med. Soc. Magn. Reson. Med.* 62, 754–762.
1137 <https://doi.org/10.1002/mrm.22028>
- 1138 Zhang, H., Schneider, T., Wheeler-Kingshott, C.A., Alexander, D.C., 2012. NODDI: Practical in vivo
1139 neurite orientation dispersion and density imaging of the human brain. *NeuroImage* 61,
1140 1000–1016. <https://doi.org/10.1016/j.neuroimage.2012.03.072>
- 1141 Zhang, Y., Brady, M., Smith, S., 2001. Segmentation of brain MR images through a hidden Markov
1142 random field model and the expectation-maximization algorithm. *IEEE Trans. Med. Imaging*
1143 20, 45–57. <https://doi.org/10.1109/42.906424>
- 1144